

# Molecular Line Profile Fitting with Analytic Radiative Transfer Models

Christopher H. De Vries and Philip C. Myers

*Harvard-Smithsonian Center for Astrophysics*

## ABSTRACT

We present a study of analytic models of starless cores whose line profiles have “infall asymmetry,” or blue-skewed shapes indicative of contracting motions. We compare the ability of two types of analytical radiative transfer models to reproduce the line profiles and infall speeds of centrally condensed starless cores whose infall speeds are spatially constant and range between 0 and  $0.2 \text{ km s}^{-1}$ . The model line profiles of  $\text{HCO}^+$  ( $J = 1 \rightarrow 0$ ) and  $\text{HCO}^+$  ( $J = 3 \rightarrow 2$ ) are produced by a self-consistent Monte Carlo radiative transfer code. The analytic models assume that the excitation temperature in the front of the cloud is either constant (“two-layer” model) or increases inward as a linear function of optical depth (“hill” model). Each analytic model is matched to the line profile by rapid least-squares fitting.

The blue-asymmetric line profiles with two peaks, or with a blue shifted peak and a red shifted shoulder, can be well fit by one or both of the analytic models. For two-peak profiles is best matched by the “HILL5” model (a five parameter version of the hill model), with an RMS error of  $0.01 \text{ km s}^{-1}$ , while the “TWOLAYER6” model underestimates the infall speed by a factor of  $\sim 2$ . For red-shoulder profiles, the HILL5 and TWOLAYER6 fits reproduce infall speeds equally well, with an RMS error of  $0.04 \text{ km s}^{-1}$ . The fits are most accurate when the line has a brightness temperature greater than 3 K. Our most accurate models tend to reproduce not only the line profile shape, but also match the excitation conditions along the line of sight. A better match to the line profile shape does not necessarily imply a better match to the infall speed and provide guidance on how to minimize the risk of obtaining a poor infall speed fit.

A peak signal to noise ratio of at least 30 in the molecular line observations is required for performing these analytic radiative transfer fits to the line profiles. Moderate amounts of depletion and beam smoothing do not adversely affect the accuracy of the infall speeds obtained from these models.

*Subject headings:* stars: formation — radio lines: ISM — radiative transfer

## 1. Introduction

There are four distinct stages in isolated star formation: (1) formation of a gravitationally bound core within a molecular cloud, (2) the gravitationally driven collapse of that core, (3) the formation of a central star-like object, (4) dispersal of the remaining cloud material (Shu, Adams, & Lizano 1987). The initial two stages are predominantly studied through millimeter- and submillimeter-wave-length observations. The molecular line rotational transition emission visible in these wavelength regimes allow one to probe both the physical and chemical composition of the molecular cloud cores out of which stars form. Spectral analysis of the molecular line emission also allows one to investigate the kinematic motions within the molecular cloud, particularly the phase of gravitational collapse (Myers et al. 2000) as well as the associated bipolar outflows which are ubiquitous around young stars (Bachiller 1996).

In a dense cloud core, commonly used molecular line tracers of moderate optical depth, such as CS ( $J = 2 \rightarrow 1$ ), or HCO<sup>+</sup> ( $J = 1 \rightarrow 0$ ) tend to become self-absorbed. As the cloud contracts under the influence of gravity, the central regions tend to become more dense than the outer regions. This sets up a gradient in the excitation temperature of the molecular gas within the cloud such that the excitation temperatures in the central regions of the cloud are greater than those in the outer regions, even if the kinetic temperature is constant within the molecular cloud. If the cloud is spherical and static the spectral line emission from this cloud in these tracers will be symmetric about the line of sight velocity and self-absorbed. However, if there is radial motion around the molecular cloud core, a velocity gradient develops around the center of the core, precisely where the excitation temperature is the greatest. Much of the emission from the rear of the cloud is not absorbed as it travels through the core, due to the high excitation temperature within the core, and continues unabsorbed through the front section of the cloud because the velocity gradient between the rear and front sections of the cloud results in a Doppler shift which is significant compared to the broadening by thermal motions. Emission from the front of the cloud however is absorbed by nearby molecular gas with lower excitation temperature and only a small Doppler shift. In the case of inward radial motion the rear emission is blue-shifted and the front emission is red-shifted, yielding the “classic” blue-asymmetric infall line profile. This line profile has become the predominant tool for investigating infall motions within star-forming molecular cloud cores (Snell & Loren 1977; Zhou 1992, 1995; Mardones et al. 1997; Gregersen et al. 2000; Lee et al. 2001).

Although this blue-asymmetry results from infall, it is not unique to that phenomenon. The superposition of multiple clouds along the line of sight can also cause an asymmetric line profile. By observing an optically thin molecular line, which should remain symmetric around the line of sight velocity of the cloud core, it is possible to reduce the likelihood

of mistaking separate clouds for an infalling cloud. Asymmetric line profiles can also arise in kinematically complex regions. Studies have shown that rotation and outflow can also produce asymmetric line profiles (Snell et al. 1980; Adelson & Leung 1988; Narayanan et al. 2002). Even the asymmetric line emission of B335, once thought to be the prototypical example of spectrally detected inside-out collapse (Zhou et al. 1993, 1994; Zhou 1995), is now also thought to also contain an outflow which gives rise to the line wings previously modeled as part of the collapse (Wilner et al. 2000). In spite of the multiple molecular cloud configurations that can result in blue-asymmetric line profiles, they are still the best way to study infall motions available, provided we understand the context in which they occur and make clear the necessary caveats.

Understanding how blue-asymmetric line profiles arise from infall motion is easy, but creating a complete model matching the molecular emission from one or more tracers is a difficult and time-consuming task. Typically one constructs an infalling physical model and uses LVG, Monte Carlo (Choi et al. 1995) or microturbulent (Zhou 1995) radiative transfer to model the emission. By iteratively changing the model parameters one is able to match some or all of the observations reasonably well. This process can take several minutes per iteration, and becomes prohibitively slow as the number of physical parameters becomes large and as the number of molecular species increases. The derived cloud parameters are also highly dependent on the input physical model. Changing the physical model can lead to an entirely different set of solutions.

“Starless cores” are useful regions for observations of inward motion because they are numerous, nearby, relatively simple in their density structure, and their motions are not confused by outflows. They have been the subject of several studies (Lee & Myers 1999; Lee et al. 1999, 2001; Bacmann et al. 2000; Murphy & Myers 2003; Tafalla et al. 2002, 2004; Tafalla & Santiago 2004; Park et al. 2004), some of which have used radiative transfer models to fit their line profiles. In this paper we present simple analytic radiative transfer models, based on the simplest available assumptions of possible excitation temperature trends within starless molecular cloud cores. These models can easily be fit to blue-asymmetric self-absorbed molecular line profiles, and produce an estimate of the infall velocity suggested by those line profiles. We also test the efficacy of the analytic radiative transfer models by comparing the infall velocities derived using those models with actual infall velocities in rigorously modeled condensing molecular clouds. Our main finding is that our analytic radiative transfer models can yield good estimates for the physical conditions of the starless cores with few assumptions and little computational investment.

## 2. Analytic Models

We compare two analytic models in this paper. Although it is possible to construct more analytic models using the same techniques in this paper we feel that these two models are the most appropriate for modeling infall. It is possible to analytically integrate the equation of transfer

$$\frac{dT_{\text{B}}}{d\tau_{\nu}} = -T_{\text{B}} + J(T), \quad (1)$$

where  $T_{\text{B}}$  is the brightness temperature,  $T$  is the excitation temperature and  $J(T) = (h\nu/k) [\exp(h\nu/kT) - 1]^{-1}$ . The brightness temperature is defined as  $T_{\text{B}} = (c^2/2\nu^2k) I_{\nu}$  and is directly proportional to the specific intensity  $I_{\nu}$ . The general solution to the equation of transfer, assuming that optical depth increases away from the observer is

$$T_{\text{B}} = T_i e^{-\tau_0} + \int_0^{\tau_0} J(T) e^{-\tau} d\tau, \quad (2)$$

where  $T$  is the excitation temperature of a region which varies over the optical depth interval from 0 to  $\tau_0$ , and  $T_i$  is the incident specific intensity of radiation on that region at  $\tau_0$  in units of brightness temperature. This equation can easily be integrated over regions of constant excitation temperature. We assume regions of constant excitation temperature along the line of sight in our first model.

The first model, first discussed in Myers et al. (1996), we call the “two-layer” model. It is perhaps unfortunate that this name has been given to this model and has stuck, as it implies that this is a model of two plane-parallel layers along the line of sight. This is not true. The model actually applies to a line of sight in which two regions with differing excitation temperatures are moving toward each other. We assume the near region has a lower excitation temperature than the far region. We assume both regions have a velocity dispersion for the observed molecule  $\sigma$  and a total optical depth of  $\tau_0$  at line center. The excitation temperature of the front region is  $T_f$ , while that of the rear region is  $T_r$ , and the regions are approaching each other with a speed of  $2v_{\text{in}}$ . The optical depth of each region at a velocity  $v$  is

$$\tau_f(v) = \tau_0 \exp \left[ -(v - v_{\text{LSR}} - v_{\text{in}})^2 / 2\sigma^2 \right], \quad (3)$$

$$\tau_r(v) = \tau_0 \exp \left[ -(v - v_{\text{LSR}} + v_{\text{in}})^2 / 2\sigma^2 \right], \quad (4)$$

assuming that the average line of sight velocity of both regions is  $v_{\text{LSR}}$ . Figure 1 provides a graphical representation of the model. The brightness temperature of the spectral line, obtained from the equation of radiative transfer, is

$$\Delta T_{\text{B}}(v) = J(T_f) [1 - e^{-\tau_f(v)}] + J(T_r) [1 - e^{-\tau_r(v)}] e^{-\tau_f(v)} - J(T_b) [1 - e^{-\tau_r(v) - \tau_f(v)}], \quad (5)$$

where  $T_b$  is the background temperature. The parameters  $\tau_0$ ,  $\sigma$ ,  $T_f$ ,  $T_r$ ,  $v_{\text{LSR}}$ , and  $v_{\text{in}}$  are free parameters which can be adjusted to fit blue-asymmetric line profiles. Lee et al. (2001) has used this analytic model to derive infall velocity estimates for 29 starless cores. They find that infall velocities are typically on the order of a tenth of a kilometer per second, comparable to the velocity dispersions measured in these sources.

Equation 2 is also analytically integrable if  $J(T)$  is a linear function of the optical depth  $\tau$ . Assuming a simple linear function  $J(T) = J_1 + [(J_2 - J_1)/\tau_0]\tau$  we can integrate the equation of transfer to obtain

$$T_B = T_i e^{-\tau_0} + (J_2 - J_1) \frac{1 - e^{-\tau_0}}{\tau_0} + J_1 - J_2 e^{-\tau_0}. \quad (6)$$

In the above equation  $\tau$  is a function of the Doppler velocity, so in order to calculate the intensity of emission across a line profile  $J(T)$  must be a linear function of  $\tau$  at every frequency. It is possible to construct a series of regions along the line of sight where  $J(T)$  varies linearly with  $\tau$  within each region and analytically calculate the brightness of radiation at a given frequency emitted from that line of sight using the above equation. We have constructed our next model using the above technique and equations which we feel approximates the excitation conditions seen along the line of sight in infalling clouds.

The second model, which we call the “hill” model, is introduced for the first time in this paper. This model consists of a core with a peak excitation temperature  $T_P$  at the center and an excitation temperature of  $T_0$  at the near and far edges of the core. The  $J(T)$  drops linearly from  $J(T_P)$  at the center to  $J(T_0)$  at edges of the core, forming a hill in the  $J(T)$  profile. The optical depth of the core is  $\tau_C$ , and its infall velocity is  $v_C$ , while the systematic velocity of the system is  $v_{\text{LSR}}$ . A schematic representation of this model is shown in figure 1. We introduce this new type of model because we believe it may be more analogous to the excitation profile we are likely to be observing in starless cores. In figure 2 we compare the excitation profile as a function of optical depth at line center for a simulated cloud, based on a Monte Carlo radiative transfer model, to the best fit hill and two-layer models of the line profile derived from that cloud. The excitation profile of our modeled starless core has a significant slope, which the hill model can replicate, but the two-layer model, due to its use of constant excitation temperature zones, can not replicate. This improvement provides motivation for introducing a new analytic radiative transfer model of infall.

In order to solve the equation of radiative transfer we separate the hill model profile into two regions along the line of sight: (1) The portion of the cloud in which the excitation temperature is rising along the line of sight, whose optical depth is  $\tau_f$ ; And (2) The portion of the cloud in which the excitation temperature is falling along the line of sight, whose optical depth is  $\tau_r$ . The optical depth as a function of line of sight velocity for each of these

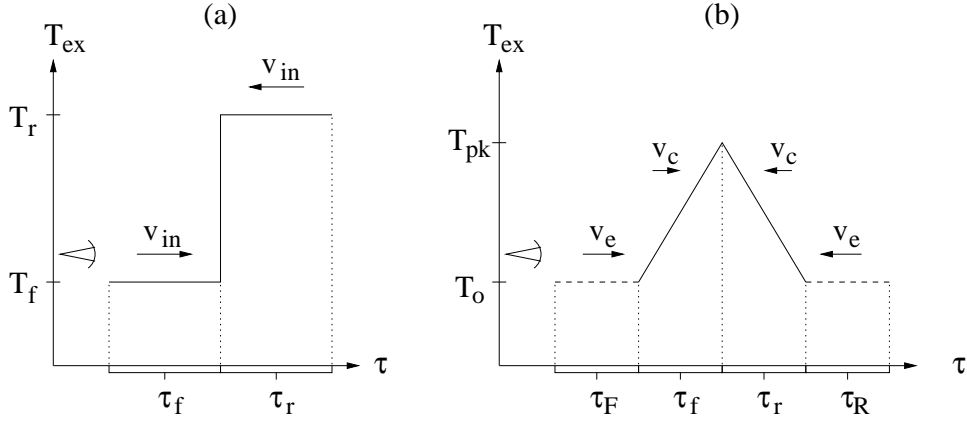


Fig. 1.— Graphical representation of the analytic radiative transfer models utilized in this paper. Each graph indicates the excitation temperature for a line transition as a function of optical depth at some frequency. Graph (a) is the two-layer model, which has a constant excitation temperature  $T_f$  for an optical depth of  $\tau_f$  and a higher excitation temperature  $T_r$  for an optical depth of  $\tau_r$ . Each region of constant excitation is traveling at velocity  $v_{\text{in}}$  toward the other region. The symbol in the left indicates the position of the observer and the arrows indicate the direction of motion relative to the observer of each region. Graph (b) is the hill model, which has an optional envelope of constant excitation temperature  $T_o$  with an optical depth of  $\tau_F$  on the side close to the observer, and optical depth  $\tau_R$  on the side opposite the observer (shown in dashed lines). In the core of the hill model the  $J(T)$  rises linearly from  $J(T_0)$  to  $J(T_{\text{pk}})$  over an optical depth of  $\tau_f$  and then falls again to  $J(T_0)$  over an optical depth of  $\tau_f$ . In the Rayleigh-Jeans limit  $J(T)$  is equal to the excitation temperature and the excitation profile is as depicted, however at higher frequencies the lines rising to  $T_{\text{pk}}$  would have some curvature.

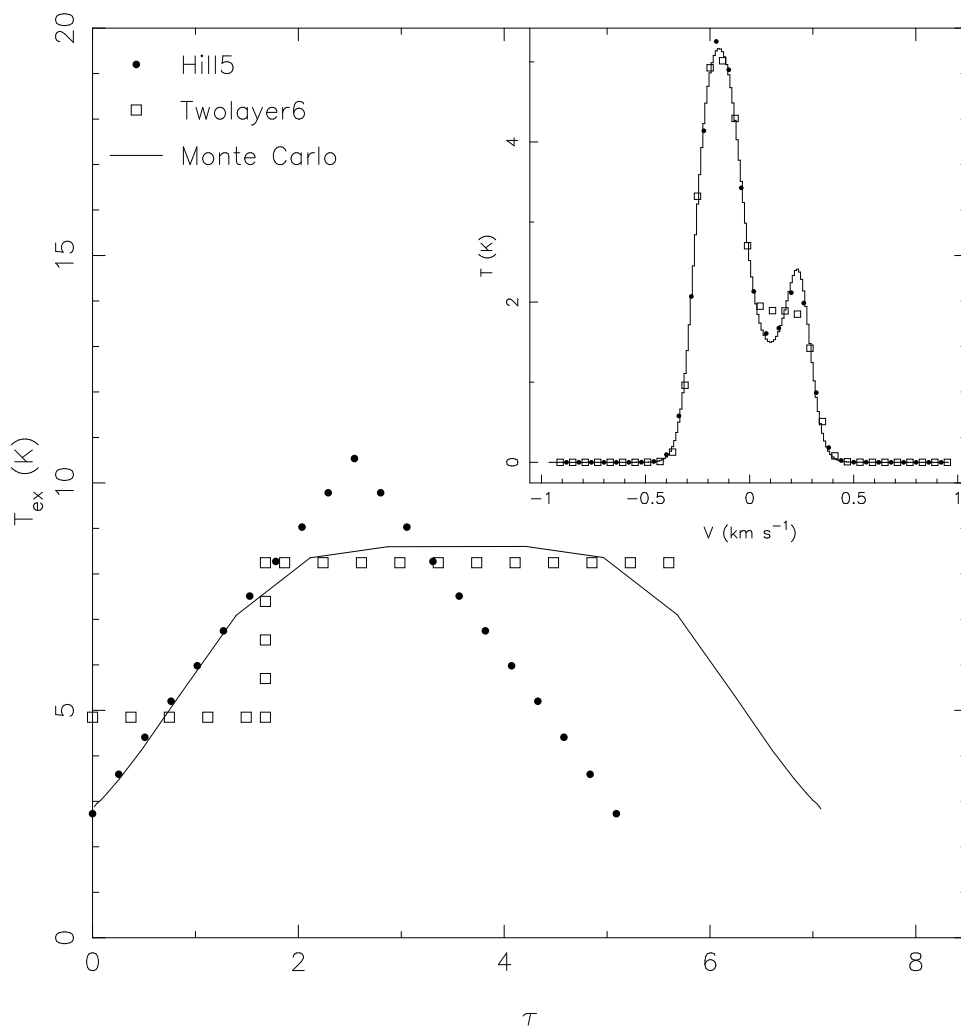


Fig. 2.— Line excitation temperature versus line center optical depth for three radiative transfer models. The solid line indicates the excitation temperature as a function of optical depth for the  $\text{HCO}^+$  ( $J = 1 \rightarrow 0$ ) transition at line center in a starless cloud core whose density follows the expression  $n(r) = n_0/[1 + (r/r_0)^\alpha]$ , with  $\alpha$  of 4, and  $r_0$  of  $5 \times 10^{16}$  cm. The cloud has an velocity dispersion of  $0.1 \text{ km s}^{-1}$  as well as a constant infall at all radii of  $0.1 \text{ km s}^{-1}$ . The  $\text{HCO}^+$  ( $J = 1 \rightarrow 0$ ) line profile generated using the Hogerheijde & van der Tak (2000) radiative transfer model is shown in the upper right corner of the figure. The filled circles indicate the excitation profile of the best HILL5 fit to the emerging line profile of that cloud, while the open squares indicate the excitation profile of the best TWOLAYER6 model fit to the emerging line profile of this simulated starless core. The line profiles generated by these models are shown in the upper right hand corner of the figure.

regions is

$$\tau_f(v) = \tau_C \exp \left[ -(v - v_{\text{LSR}} - v_C)^2 / 2\sigma^2 \right], \quad (7)$$

$$\tau_r(v) = \tau_C \exp \left[ -(v - v_{\text{LSR}} + v_C)^2 / 2\sigma^2 \right], \quad (8)$$

assuming a velocity dispersion of  $\sigma$  in the entire cloud. We can now solve the equation of transfer by integrating along the line of sight through each of these two regions to derive the brightness temperature

$$\begin{aligned} \Delta T_{\text{B}}(v) = & (J(T_P) - J(T_0)) \left[ (1 - e^{-\tau_f(v)}) / \tau_f(v) - e^{-\tau_f(v)} (1 - e^{-\tau_r(v)}) / \tau_r(v) \right] \\ & + (J(T_0) - J(T_b)) \left[ 1 - e^{-\tau_r(v) - \tau_f(v)} \right], \end{aligned} \quad (9)$$

where  $T_b$  is the background temperature. We believe the excitation temperature gradient in this model might more closely approximate the excitation profiles in observed clouds. The six free parameters in the hill model are  $\tau_C$ ,  $\sigma$ ,  $T_0$ ,  $T_P$ ,  $v_{\text{LSR}}$ , and  $v_C$ . It is also possible to add an envelope of constant excitation temperature moving with its own infall velocity. Assuming this envelope has an excitation temperature of  $T_0$ , the optical depth of the envelope and the velocity of the envelope adds two more free parameters, creating a maximum of eight free parameters possible in the hill models.

In order to reduce the total number of free parameters we consider several variants of each model by holding certain parameters fixed. We considered two variants of the two-layer model, which we call TWOLAYER5 and TWOLAYER6, as well as 4 variants of the hill model, which we call HILL5, HILL6, HILL6CORE, and HILL7. The number in each variant name refers to the number of free parameters in that variant. The parameterization of the two-layer model variants are shown in table 1, while those of the hill model variants are shown in table 2.

### 3. Physical Models

The analytic radiative transfer models do an excellent job of fitting blue-asymmetric line profiles (Lee et al. 2001). Their efficacy in determining physical parameters of the molecular cloud, such as infall velocity, has not yet been studied. In this paper we study how effectively we can recover the physical parameters of modeled clouds using both the two-layer and hill analytic radiative transfer models. We then use this information to determine the point at which the systematic errors of the model dominate over random observational errors.

In our first three simulations, we modeled molecular clouds with a density law of the form

$$n(r) = \frac{n_0}{1 + (r/r_0)^\alpha}, \quad (10)$$



Table 1. Variants of the two-layer model

Variant Name	$\tau_0$	$v_{\text{LSR}}$	$v_{\text{in}}$	$\sigma$	$T_f$	$T_r$
TWOLAYER5	Free	Free	Free	Free	$T_b$	Free
TWOLAYER6	Free	Free	Free	Free	Free	Free

Note. —  $\tau_0$  is the line center optical depth,  $v_{\text{LSR}}$  is the line of sight velocity of the system,  $v_{\text{in}}$  is the infall velocity of the system,  $\sigma$  is the velocity dispersion of the molecular species,  $T_f$  is the excitation temperature of the front layer, and  $T_r$  is the excitation temperature of the rear layer.

Table 2. Variants of the hill model

Variant Name	$\tau_E$	$\tau_C$	$v_{\text{LSR}}$	$v_E$	$v_C$	$\sigma$	$T_0$	$T_{\text{pk}}$
HILL5	0	Free	Free	0	Free	Free	$T_b$	Free
HILL6	Free	Free	Free	Free	0	Free	$T_b$	Free
HILL6CORE	Free	Free	Free	0	Free	Free	$T_b$	Free
HILL7	Free	Free	Free	Free	0	Free	Free	Free

Note. —  $\tau_E$  is the line center optical depth of the optional envelope,  $\tau_C$  is the line center optical depth of the cloud,  $v_{\text{LSR}}$  is the line of sight velocity of the system,  $v_E$  is the infall velocity of the envelope,  $v_C$  is the infall velocity of the cloud,  $\sigma$  is the velocity dispersion of the molecular species,  $T_0$  is the excitation temperature of the edge of the cloud as well as the optional envelope, and  $T_{\text{pk}}$  is the peak excitation temperature in the cloud.

where  $n_0$  is the central density,  $r_0$  is the turnover radius, and  $\alpha$  is the power law of the density profile at large radii (Tafalla et al. 2002). This model reproduces the flat density region (at  $r < r_0$ ) and power law region (at  $r > r_0$ ) required to model starless cores. It also is in good agreement with the density profile of a Bonnor-Ebert sphere (Tafalla et al. 2004) as well as the “Plummer-like” density model of Whitworth & Ward-Thompson (2001). The clouds modeled in this paper have peak densities ( $n_0$ ) of  $6 \times 10^4 \text{ cm}^{-3}$ , a turnover radius ( $r_0$ ) of  $5 \times 10^{16} \text{ cm}$ , an outer radius of  $2 \times 10^{17} \text{ cm}$ , and an  $\alpha$  of 4. We chose to model  $\text{HCO}^+$  rotational line emission from these clouds, as it is often moderately optically thick in starless cores. We assumed that the kinetic temperature of the gas is 10 K throughout the cloud. We set the relative abundance of  $\text{HCO}^+$  at  $2 \times 10^{-9}$  (van Dishoeck et al. 1995) and the  $\text{HCO}^+/\text{H}^{13}\text{CO}^+$  abundance ratio to 64. Depletion is not included here, however we do investigate the effect of depletion in §4.6. There are four velocity laws which we investigate in this paper. The first (Simulation A) is constant infall velocity for all radii in the cloud. The second (Simulation B) is a constant infall velocity for  $r > r_0$  and 0 velocity for  $r < r_0$ . The third (Simulation C) is constant infall velocity for  $r < r_0$  and 0 velocity for  $r > r_0$ . These simulations are summarized in Table 3. These velocity laws were chosen because they are simple velocity laws to investigate. Our analytic radiative transfer models define a characteristic single infall velocity which is analogous to Simulations A, B, and C. We set the velocity dispersion to  $0.1 \text{ km s}^{-1}$  over the entire cloud and typically allow the velocities within the cloud to be up to twice the velocity dispersion. These results should all scale with the velocity dispersion and the peak line brightness. In addition to the simulations described above, we also simulated a different density profile based on the best fit Bonnor-Ebert model of B68 (Alves et al. 2001). The parameters of this simulation (Simulation D) are discussed in §4.4.

We use these simulated starless cloud cores to synthesize  $\text{HCO}^+$  ( $J = 1 \rightarrow 0$ ) and  $\text{HCO}^+$  ( $J = 3 \rightarrow 2$ ) molecular line emission using the Hogerheijde & van der Tak (2000) 1-D Monte Carlo radiative transfer model. The simulated clouds were divided into 20 spherical shells, each of uniform density, kinetic temperature, radial velocity, and with a radial size of  $10^{16} \text{ cm}$ . The level populations within the first 21 rotational levels of the  $\text{HCO}^+$  molecule were calculated using the Einstein-A and  $\text{HCO}^+$  with  $\text{H}_2$  collisional rate coefficients from Monteiro (1985) and Green (1975). We then integrate along the central line of sight to find the  $J = 1 \rightarrow 0$  and  $J = 3 \rightarrow 2$  molecular line spectral profiles of  $\text{HCO}^+$  because they are frequently observed, and often have blue-asymmetric line profiles attributed to infall (Gregersen et al. 1997; Narayanan & Walker 1998; Narayanan et al. 1998, 2002; De Vries et al. 2002). We then fit these synthesized spectra with the two-layer and hill analytic radiative transfer models to check the ability of the analytic models to recover physical parameters within the modeled cloud.

Several algorithms exist for minimizing multidimensional functions. There is always the danger of minimizing to a “local” minimum (meaning the lowest value within some finite region of the function to be minimized) instead of the “global” minimum (meaning the lowest function value over the entire parameter space) and it becomes more difficult to avoid local minima as your function goes to higher dimensions. There are several strategies to avoid local minima, and we have chosen a hybrid minimization algorithm to do just that. We use the Differential Evolution (DE) algorithm of Storn & Price (1997) initially to separate the local minima from the global minimum, then we use the Nelder-Mead simplex method (Nelder & Mead 1965) to optimize the fit. The DE minimization algorithm is applicable to many astronomical problems, and is similar in scope to simulated annealing. DE is an evolutionary algorithm in that several parameter sets are randomly selected and these are randomly modified over several “generations” until acceptable convergence has been achieved. The variability in each parameter is scaled by the variation of the solution sets in each generation, so as the algorithm converges the region of the search decreases without the need to include a decreasing “temperature” as in simulated annealing. DE is also superior to simulated annealing in that it is more likely to achieve convergence, is a simpler algorithm, and has fewer adjustable parameters (Storn & Price 1997).

## 4. Results

We made four simulations of infalling clouds and used the Hogerheijde & van der Tak (2000) Monte Carlo radiative transfer model to extract  $\text{HCO}^+$  ( $J = 1 \rightarrow 0$ ) and  $\text{HCO}^+$  ( $J = 3 \rightarrow 2$ ) line profiles from those simulations. In this section we will discuss how effective our analytic models are at deriving the input velocities in those simulation, quantify the relative contributions of both random and systematic errors in model fits of simulated data sets, and apply this model to an observed infall profile in a source which has been rigorously modeled using Monte Carlo radiative transfer techniques.

### 4.1. Simulation A — Constant Infall

Simulation A, which has a constant infall velocity for all cloud radii, has asymmetric line profile typical of those seen in infalling clouds. The  $\text{HCO}^+$  ( $J = 1 \rightarrow 0$ ) line profiles are shown in figure 3, along with their optically thin  $\text{H}^{13}\text{CO}^+$  ( $J = 1 \rightarrow 0$ ) counterparts. The spectra in the bottom on the left and right side are for a simulation with no infall. The middle spectra on the left and right are of a simulation with an infall velocity of  $0.1 \text{ km s}^{-1}$ . The top spectra on the left and right are from a simulation with an infall velocity of  $0.2 \text{ km s}^{-1}$ .

Overlain on the  $\text{HCO}^+$  ( $J = 1 \rightarrow 0$ ) spectra on the left panel are the TWOLAYER5 and HILL5 best fit models, while on the right the TWOLAYER6 and HILL6 spectra are shown. Figure 4 depicts  $\text{HCO}^+$  ( $J = 3 \rightarrow 2$ ) and  $\text{H}^{13}\text{CO}^+$  ( $J = 3 \rightarrow 2$ ) spectra from the same simulations along with their TWOLAYER5, HILL5, TWOLAYER6, and HILL6 best fit spectral line profiles. Two variants are not shown in these fits, the HILL6CORE model best fit in most cases has a  $\tau_E$  which is very close to 0, yielding the same parameters and spectral line shape as the HILL5 model. The HILL7 model always manages a very good fit to the spectral line shape, however in some cases, especially in spectra with a small red component that is not well separated from the blue component (such as the middle and top spectra in figure 4), the parameters of the HILL7 model are not very well constrained. A wide range of infall velocities, optical depths, and excitation temperatures in the seven parameter HILL7 model can yield the same line profile.

There are several interesting features in these spectral line fits. When the infall velocity is greater than the velocity dispersion the  $\text{H}^{13}\text{CO}^+$  line profiles become double peaked. This is not due to self-absorption as the lines are optically thin. It is due to the fact that the molecular gas along the central line of sight is traveling at two velocities separated by more than the velocity dispersion, resulting in two peaks in the optically thin component. This feature is unlikely to be observed in  $\text{H}^{13}\text{CO}^+$  ( $J = 3 \rightarrow 2$ ) lines as they are too weak to be easily detected. Also interesting is that while the dip between the red and blue peaks of the spectral line profile is deep, both the hill variants and the two-layer variants do a good job a reproducing the spectral line, but as the red peak drops in intensity relative to the blue peak the analytic model fits tend to produce a spectral line with a single blue peak and a red shoulder with no local maximum but only a flattening of the slope. The two-layer model variants tend to produce this type of spectrum at lower infall speeds than the hill model variants (Figure 3). We call the spectra with distinct blue and red peaks “dip” spectra and those with only a flattening of the slope, “shoulder” spectra. We also see that none of the models can reproduce a spectral line which has a minimal red peak superimposed on a broadly asymmetric line (as in the top spectra of figure 4). These models tend to produce spectra that are similar in shape to two overlapping gaussians of equal width. If we try to fit a spectral line that differs greatly from one that can be obtained by adding two gaussians of equal width, then we tend to not get good line fits with any of the analytic models.

In figure 5 we show the quality of the infall velocity fit attained by the analytic model fits to the  $\text{HCO}^+$  ( $J = 1 \rightarrow 0$ ) line profiles in this simulation (left side) as well as the model fits to the  $\text{HCO}^+$  ( $J = 3 \rightarrow 2$ ) line profiles in this simulation (right side). In this simulation, for the entire infall velocity range up to twice the velocity dispersion, the HILL5 model tends to reproduce the modeled infall velocity with an RMS systematic error of less than  $0.01 \text{ km s}^{-1}$  in the  $\text{HCO}^+$  ( $J = 1 \rightarrow 0$ ) lines and  $0.02 \text{ km s}^{-1}$  in the  $\text{HCO}^+$  ( $J = 3 \rightarrow 2$ )

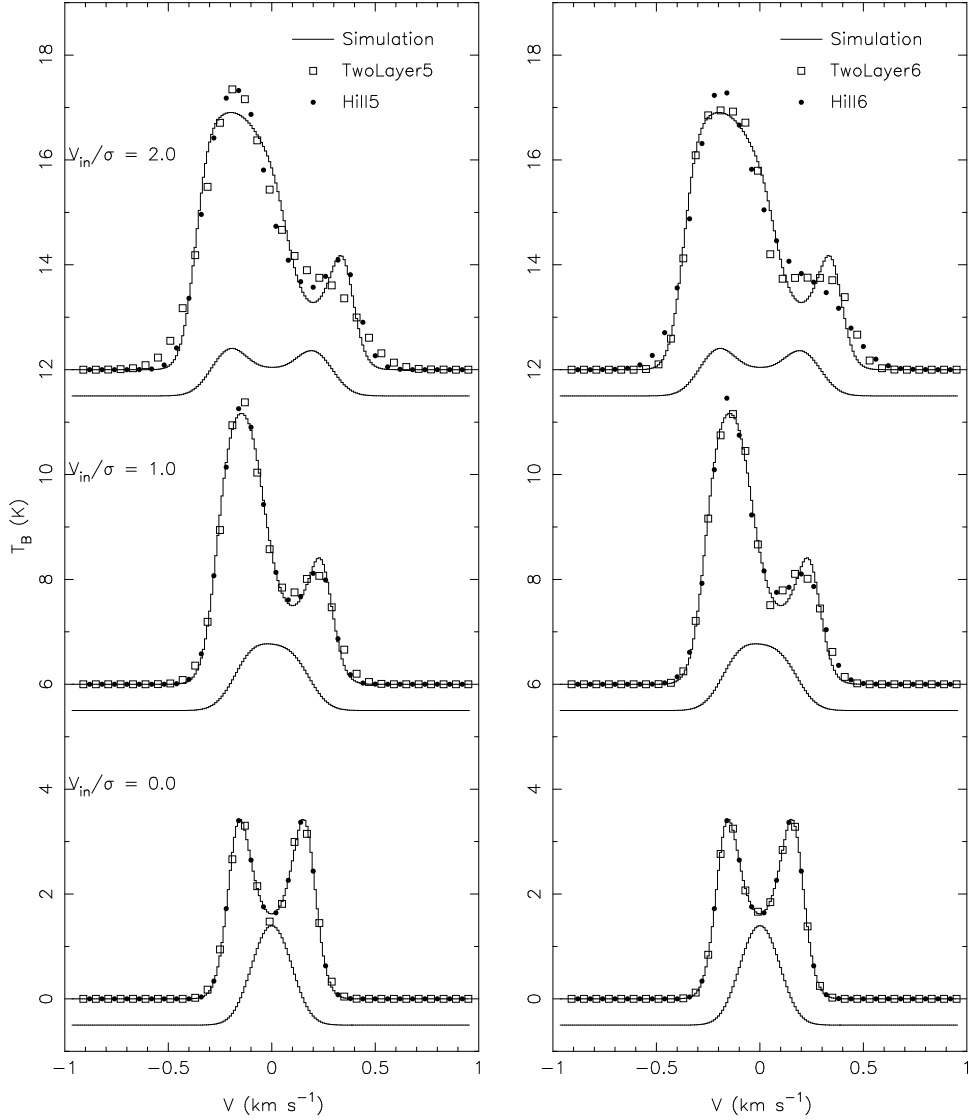


Fig. 3.— Monte Carlo simulated spectra (solid lines) of the  $\text{HCO}^+$  ( $J = 1 \rightarrow 0$ ) and  $\text{H}^{13}\text{CO}^+$  ( $J = 1 \rightarrow 0$ ) (multiplied by a factor of 5) emission from Simulation A (Constant Infall). The infall velocity in the lowest set of spectra is  $0 \text{ km s}^{-1}$ , those in the middle are of a cloud infalling at  $0.1 \text{ km s}^{-1}$ , while those at the top are of a cloud infalling at  $0.2 \text{ km s}^{-1}$ . The analytic model fits are overlaid on each  $\text{HCO}^+$  spectrum. The open squares on the left indicate the TWOLAYER5 fits, while the filled circles are the HILL5 fits. On the right the open squares indicate the TWOLAYER6 fits, while the filled circles indicate the HILL6 fit.

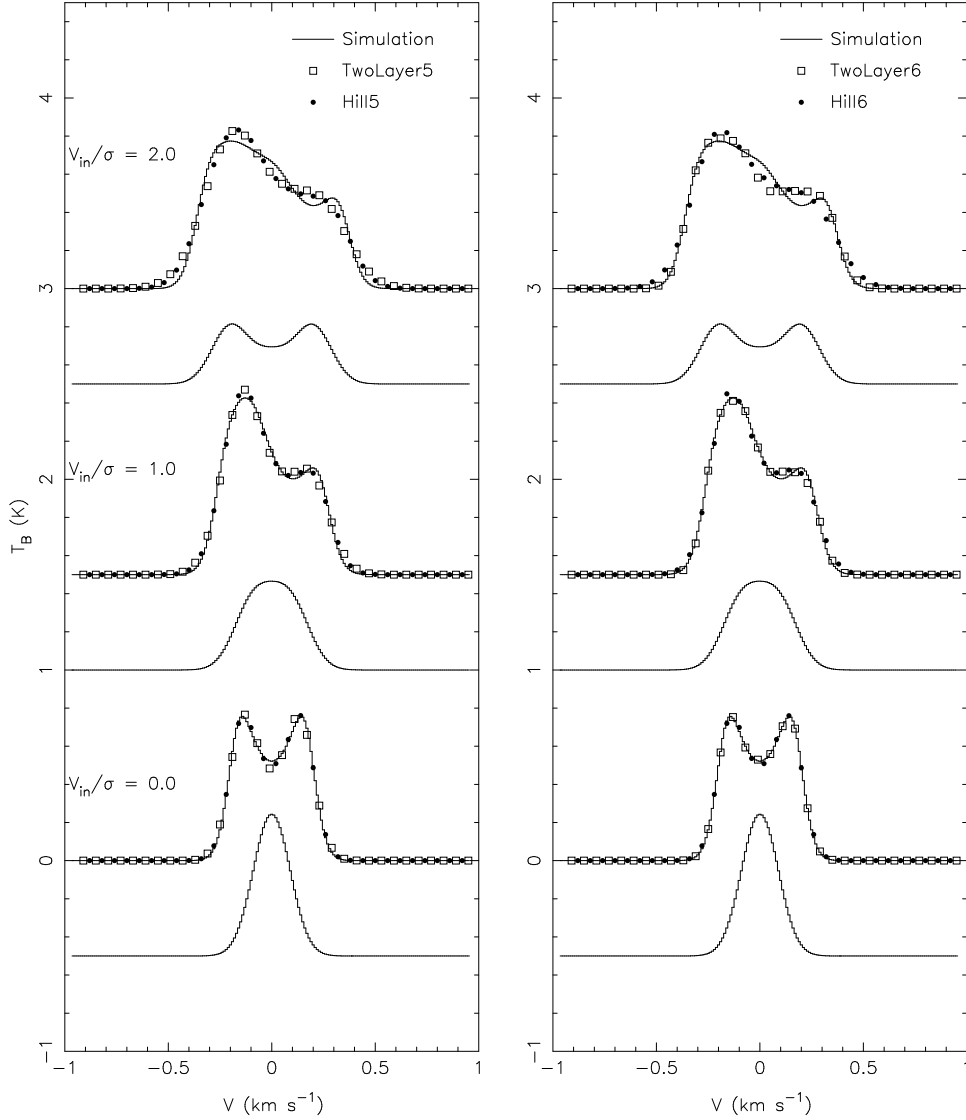


Fig. 4.— Monte Carlo simulated spectra (solid lines) of the  $\text{HCO}^+$  ( $J = 3 \rightarrow 2$ ) and  $\text{H}^{13}\text{CO}^+$  ( $J = 3 \rightarrow 2$ ) (multiplied by a factor of 40) emission from Simulation A (Constant Infall). The infall velocity in the lowest set of spectra is  $0 \text{ km s}^{-1}$ , those in the middle are of a cloud infalling at  $0.1 \text{ km s}^{-1}$ , while those at the top are of a cloud infalling at  $0.2 \text{ km s}^{-1}$ . The analytic model fits are overlaid on each  $\text{HCO}^+$  spectrum. The open squares on the left indicate the TWOLAYER5 fits, while the filled circles are the HILL5 fits. On the right the open squares indicate the TWOLAYER6 fits, while the filled circles indicate the HILL6 fit.

lines. The TWOLAYER5 model tends to consistently underestimate the infall velocity by over a factor of 2 in both transitions when it produces good line fits. The TWOLAYER6 model fits the infall velocity with an RMS error of  $0.03 \text{ km s}^{-1}$  in both the  $\text{HCO}^+$  ( $J = 1 \rightarrow 0$ ) lines and the  $\text{HCO}^+$  ( $J = 3 \rightarrow 2$ ) lines. Generally the TWOLAYER6 model does a better job in cases where the spectrum is dominated by the blue component and the relative size or integrated intensity of the red component is small. This happens to be the true for cases with higher infall velocities in the  $\text{HCO}^+$  ( $J = 1 \rightarrow 0$ ) and  $\text{HCO}^+$  ( $J = 3 \rightarrow 2$ ) spectra in this simulation. The TWOLAYER6 model also performs well when the excitation temperature of the rear layer matches the simulated excitation temperature in the cloud. The HILL6 model does a good job at fitting the infall velocity for infall velocities greater than the velocity dispersion, but tends to greatly overestimate the infall velocity in cases where it is smaller than the velocity dispersion. The HILL7 model also tends to reproduce the infall velocity fairly well, but not as well as the HILL5 model.

It should be noted that a good fit to the line profile does not always translate to a good fit to the physical parameters, such as the infall velocity, in the simulated clouds. In the case of the TWOLAYER6 models, often the dip solution is a good fit to the line profile, but a worse fit to the infall velocity than the shoulder solution. The HILL7 model is able to fit just about any line profile, but often yields worse infall velocities than HILL5 model fits with larger minimized  $\chi^2$ . In summary, the infall velocities for Simulation A (constant infall) are most accurately reproduced by the HILL5 model with a RMS deviation of  $0.016 \text{ km s}^{-1}$  over 22 cases. The TWOLAYER6 model is significantly worse with an overall RMS deviation of  $0.030 \text{ km s}^{-1}$  over 22 cases.

## 4.2. Simulation B — Envelope Infall

Simulation B, which has a constant infall velocity for  $r > r_0$  and no infall for  $r < r_0$ , has asymmetric line profiles typical of those seen in infalling clouds. Figure 6 shows the  $\text{HCO}^+$  ( $J = 1 \rightarrow 0$ ) line profiles for three different infall velocities. The self-absorbed solid line in the lowest left and right panels is the line profile for a cloud with no infall, as well as the optically thin  $\text{H}^{13}\text{CO}^+$  ( $J = 1 \rightarrow 0$ ) line profile. In the middle left and right are the  $\text{HCO}^+$  and  $\text{H}^{13}\text{CO}^+$  ( $J = 1 \rightarrow 0$ ) line profiles for a cloud with an infall velocity of  $0.1 \text{ km s}^{-1}$ , equal to the velocity dispersion in that cloud. The upper left and right panels are the  $\text{HCO}^+$  and  $\text{H}^{13}\text{CO}^+$  ( $J = 1 \rightarrow 0$ ) line profiles for a cloud with an infall velocity of  $0.2 \text{ km s}^{-1}$ . These line profiles are slightly narrower than those seen in Simulation A (Constant Infall). This is due to the fact that the cores, where the most dense gas is located, are stationary and not producing any broad line wings. As in our previous simulation we have overlaid

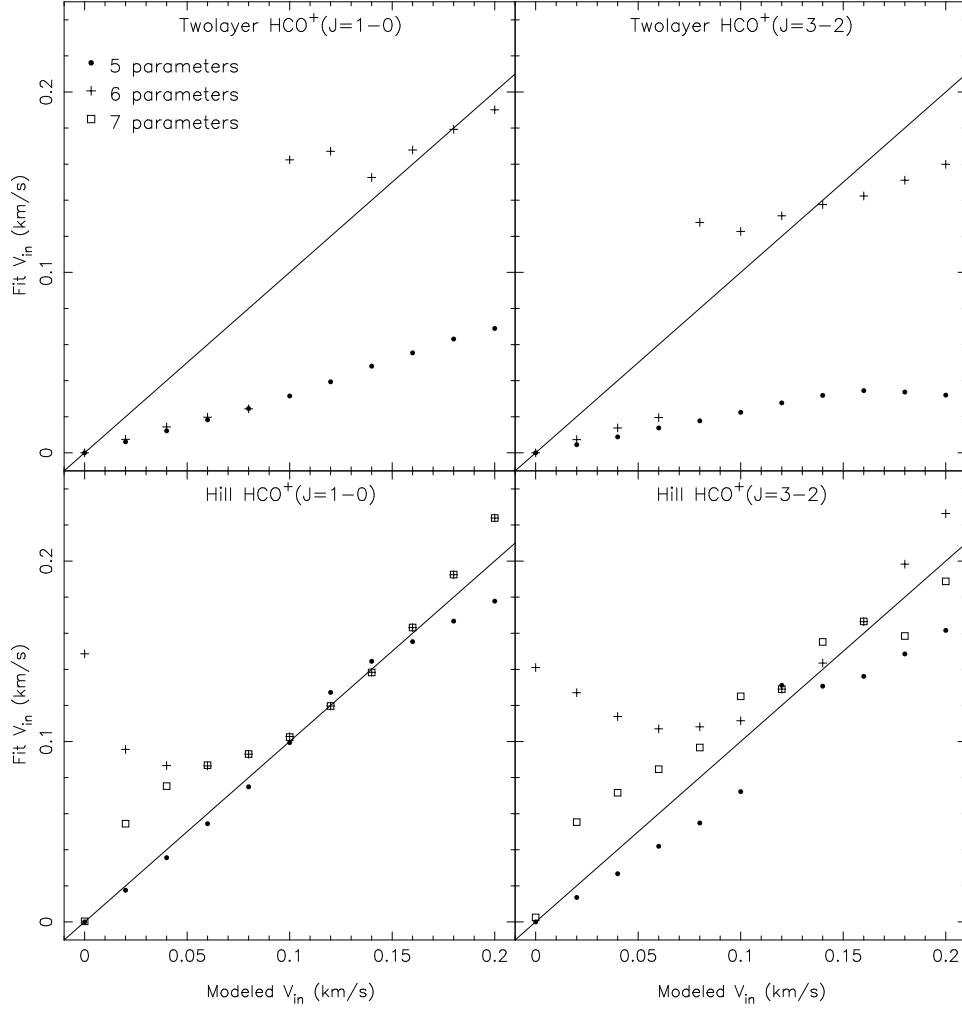


Fig. 5.— Infall velocity fits. The above figures indicate the infall velocities obtained by fitting TWOLAYER5, TWOLAYER6, HILL5, HILL6, and HILL7 models to the Monte Carlo simulated spectra in Simulation A (Constant Infall). The left hand panels are the results of fitting the  $\text{HCO}^+$  ( $J = 1 \rightarrow 0$ ) spectra, and the right hand panels are the results of fitting the  $\text{HCO}^+$  ( $J = 3 \rightarrow 2$ ) spectra. The top two figures indicate the infall velocities obtained from the two-layer models. Below the two-layer results are the results of the hill models. The symbols indicate the number of free parameters, closed circles indicate the 5 free parameter models (TWOLAYER5 and HILL5). Crosses indicate the 6 free parameter models (TWOLAYER6 and HILL6). Open squares indicate the 7 free parameter model (HILL7). The TWOLAYER6 model often has two local minima, one of which is usually fit by the TWOLAYER5 model. We show the other local minimum when it is available in this plot.



the TWOLAYER5, HILL5, TWOLAYER6, and HILL6 best fit to the  $\text{HCO}^+$  spectra. Figure 7 indicates these same results for the  $\text{HCO}^+$  ( $J = 3 \rightarrow 2$ ) and  $\text{H}^{13}\text{CO}^+$  ( $J = 3 \rightarrow 2$ ) spectra in Simulation B (Envelope Infall).

We investigate the efficacy of our models in matching the infall velocity of the Simulation B (Envelope Infall) clouds in figure 8. The TWOLAYER5 model once again underestimates the infall velocity in all cases and in both transitions, although it monotonically increases throughout the simulation. The TWOLAYER6 model tends to yield the same result as the TWOLAYER5 model over many of the infall velocities, but jumps to a higher infall velocity which in many cases approximates the correct infall velocity (especially in the  $\text{HCO}^+$  ( $J = 1 \rightarrow 0$ ) fits). We investigated these jumps in the TWOLAYER6 model further and found that there are two local minima in the  $\chi^2$  surface for many spectrum shapes.

The TWOLAYER6 minima we found correspond to “dip” spectra, with two distinct peaks, and “shoulder” spectra with one peak and a flattening of the spectrum on the red side. These two spectral line fits tend to have very different parameters for the infall velocity which we show in figure 9 for the  $\text{HCO}^+$  ( $J = 1 \rightarrow 0$ ) lines generated in this simulation. The letter with the larger size indicates the fit with the lowest  $\chi^2$ , and the solid line indicates the expected value if the infall velocity modeled analytically matches the infall velocity of the cloud. In the  $\text{HCO}^+$  ( $J = 1 \rightarrow 0$ ) profiles, the “dip” solution is a better fit to the line profile up to a modeled infall velocity of  $0.12 \text{ km s}^{-1}$ , however the “shoulder” solution yields a better fit to the infall velocity for modeled infall velocities above  $0.04 \text{ km s}^{-1}$ . A similar trend is seen in the  $\text{HCO}^+$  ( $J = 3 \rightarrow 2$ ) results. The “shoulder” fits tend to have a higher infall velocity, and are often a much better match to the infall velocity. The “dip” spectra are typically the equivalent to the TWOLAYER5 model results. The best “dip” spectrum fit of the TWOLAYER6 model usually results in an excitation temperature of the front layer equal to the background temperature and an underestimate of the infall velocity. We therefore recommend that one should attempt to find the local minimum corresponding to a “shoulder” fit when using the TWOLAYER6 model, and that one can verify that one has found the “shoulder” fit by making sure that the excitation temperature of the front layer is significantly higher than the background temperature.

Another trend revealed in figure 8 is that the TWOLAYER6 model does not do a good job of fitting high velocity infall using the  $\text{HCO}^+$  ( $J = 3 \rightarrow 2$ ) line profile in this modeled cloud. We can see in the upper-most line profiles of figure 7 that the  $\text{HCO}^+$  ( $J = 3 \rightarrow 2$ ) line profiles do not separate into multiple distinct components at high infall velocities in this model. As the lines begin to blend into a profile that is not easily separable into multiple components, the two-layer model begins to break down and does not accurately match the actual infall velocity.

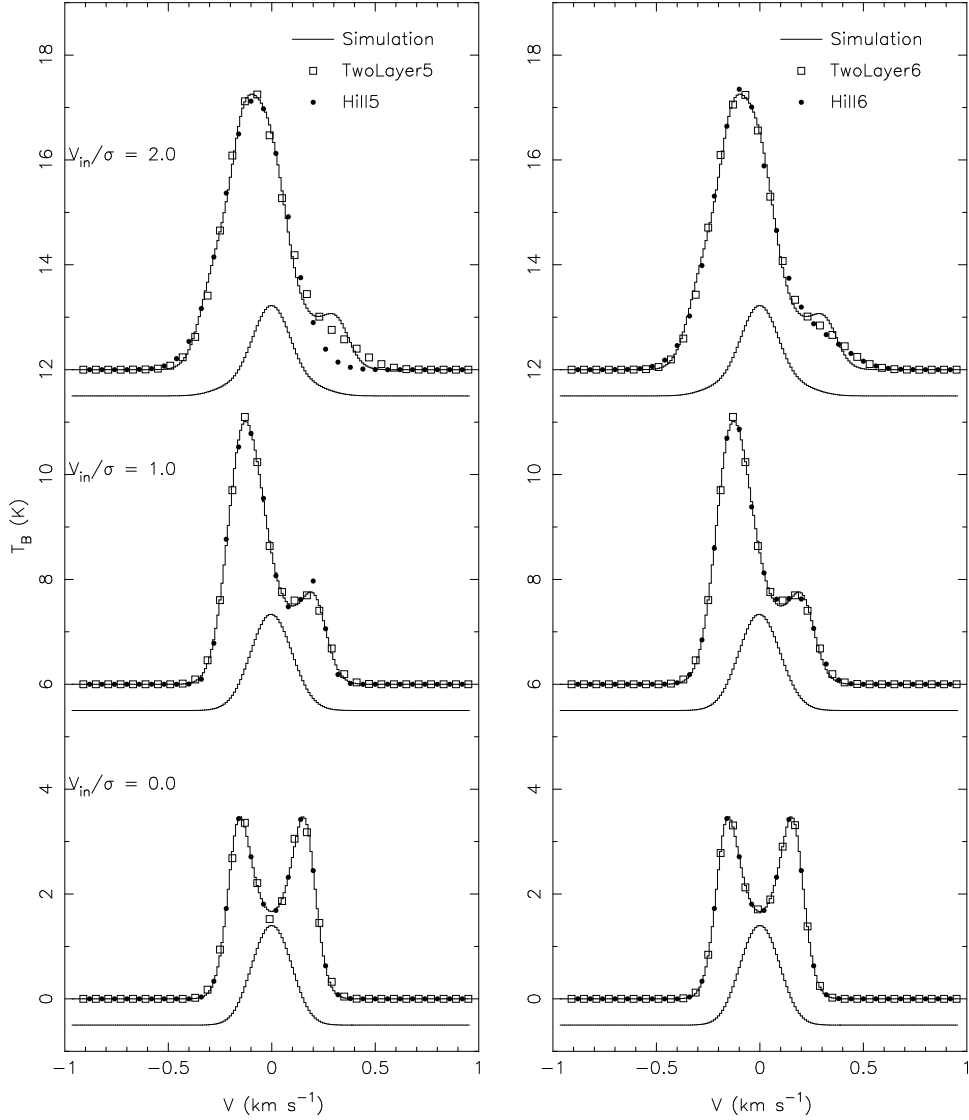


Fig. 6.— Monte Carlo simulated spectra (solid lines) of the  $\text{HCO}^+$  ( $J = 1 \rightarrow 0$ ) and  $\text{H}^{13}\text{CO}^+$  ( $J = 1 \rightarrow 0$ ) (multiplied by a factor of 5) emission from Simulation B (Envelope Infall). The infall velocity in the lowest set of spectra is  $0 \text{ km s}^{-1}$ , those in the middle are of a cloud infalling at  $0.1 \text{ km s}^{-1}$ , while those at the top are of a cloud infalling at  $0.2 \text{ km s}^{-1}$ . The analytic model fits are overlaid on each  $\text{HCO}^+$  spectrum. The open squares on the left indicate the TWOLAYER5 fits, while the filled circles are the HILL5 fits. On the right the open squares indicate the TWOLAYER6 fits, while the filled circles indicate the HILL6 fit.

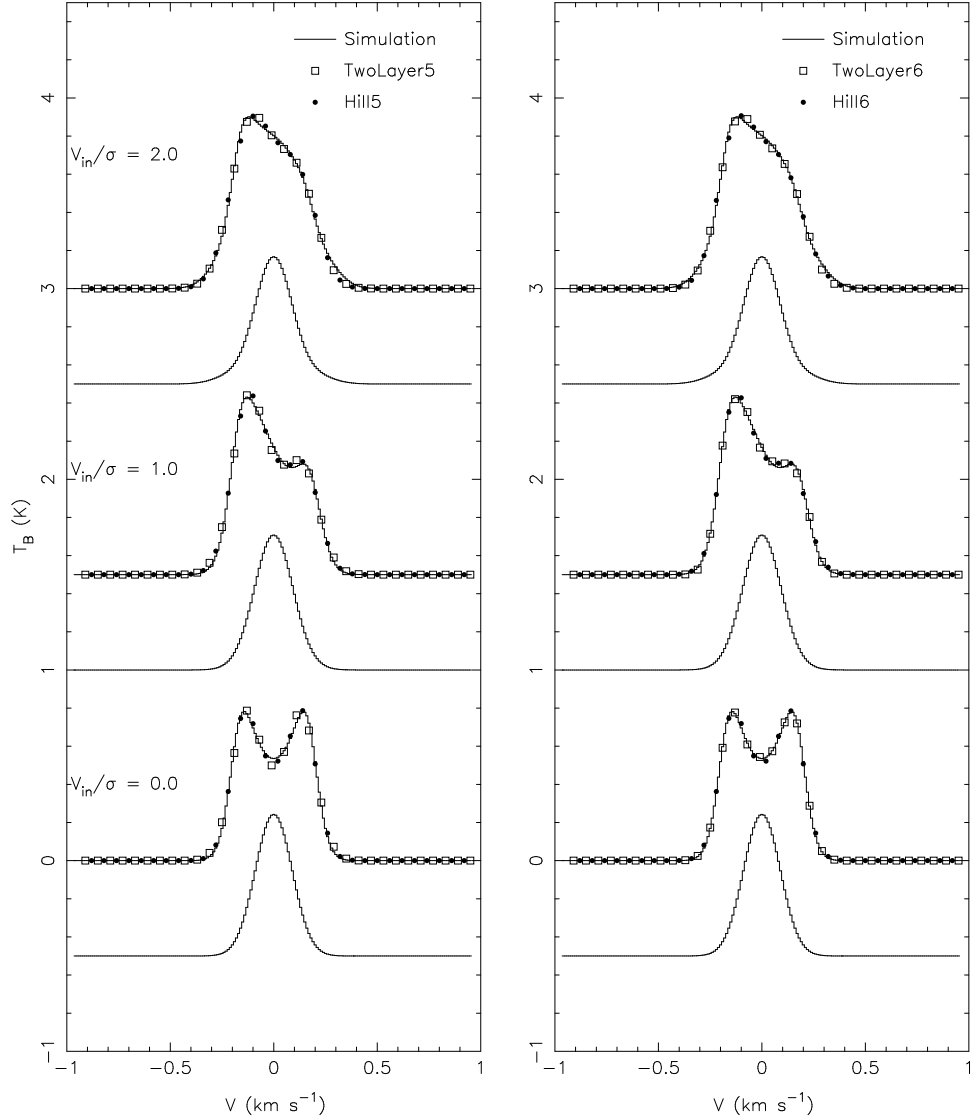


Fig. 7.— Monte Carlo simulated spectra (solid lines) of the  $\text{HCO}^+$  ( $J = 3 \rightarrow 2$ ) and  $\text{H}^{13}\text{CO}^+$  ( $J = 3 \rightarrow 2$ ) (multiplied by a factor of 40) emission from Simulation B (Envelope Infall). The infall velocity in the lowest set of spectra is  $0 \text{ km s}^{-1}$ , those in the middle are of a cloud infalling at  $0.1 \text{ km s}^{-1}$ , while those at the top are of a cloud infalling at  $0.2 \text{ km s}^{-1}$ . The analytic model fits are overlaid on each  $\text{HCO}^+$  spectrum. The open squares on the left indicate the TWOLAYER5 fits, while the filled circles are the HILL5 fits. On the right the open squares indicate the TWOLAYER6 fits, while the filled circles indicate the HILL6 fit.

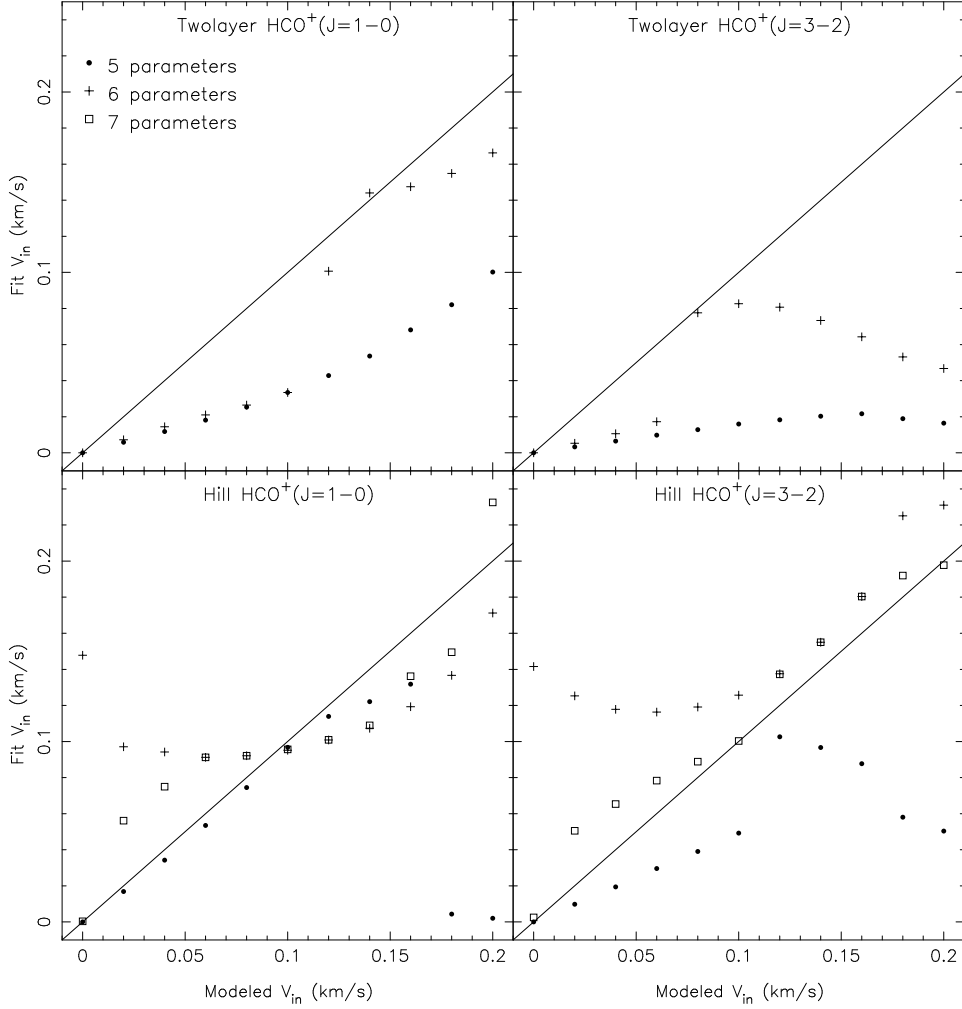


Fig. 8.— Infall velocity fits. The above figures indicate the infall velocities obtained by fitting TWOLAYER5, TWOLAYER6, HILL5, HILL6, and HILL7 models to the Monte Carlo simulated spectra in Simulation B (Envelope Infall). The left hand panels are the results of fitting the  $\text{HCO}^+$  ( $J = 1 \rightarrow 0$ ) spectra, and the right hand panels are the results of fitting the  $\text{HCO}^+$  ( $J = 3 \rightarrow 2$ ) spectra. The top two figures indicate the infall velocities obtained from the two-layer models. Below the two-layer results are the results of the hill models. The symbols indicate the number of free parameters, closed circles indicate the 5 free parameter models (TWOLAYER5 and HILL5). Crosses indicate the 6 free parameter models (TWOLAYER6 and HILL6). Open squares indicate the 7 free parameter model (HILL7). The TWOLAYER6 model often has two local minima, one of which is usually fit by the TWOLAYER5 model. We show the other local minimum when it is available in this plot.

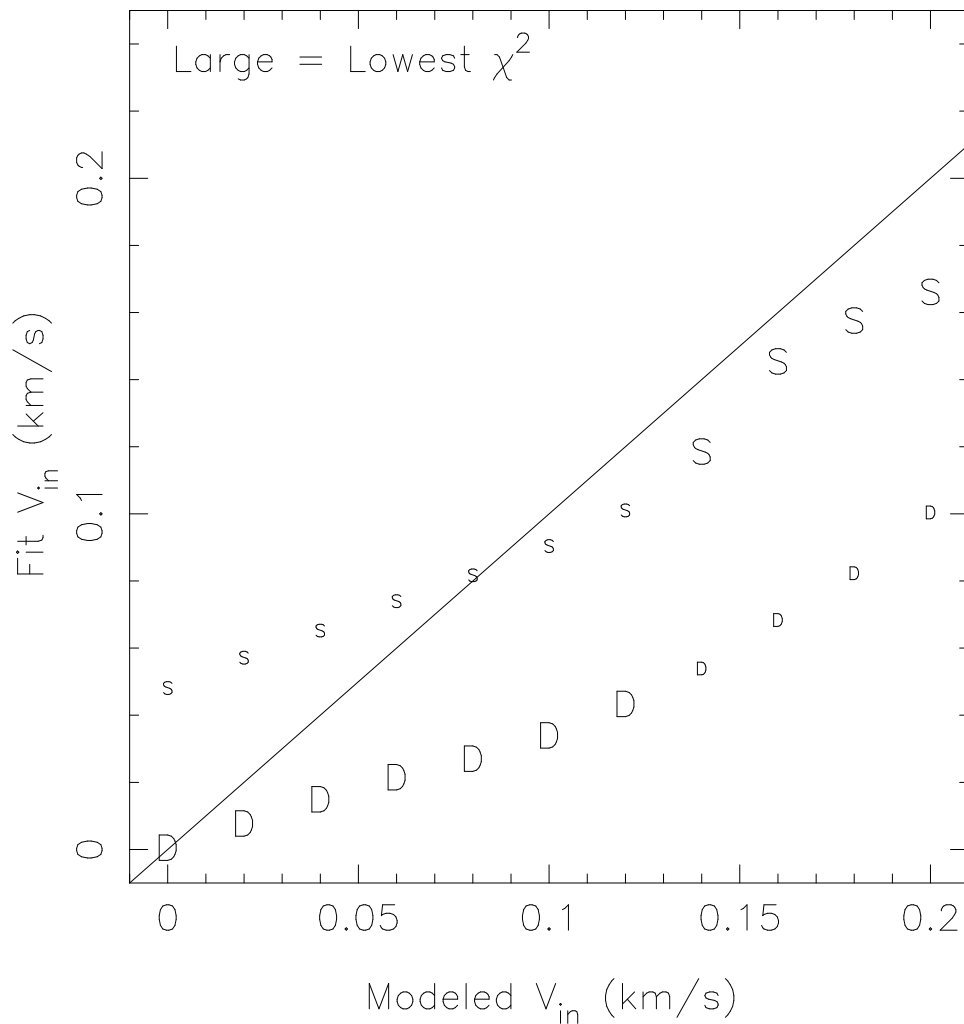


Fig. 9.— We find that there are often two local minima in the  $\chi^2$  plane of the TWOLAYER6 fit to a spectrum. We trace each local minimum for the  $\text{HCO}^+$  ( $J = 1 \rightarrow 0$ ) spectra in simulation B here. The “S” points correspond to a local minimum that tends to produce a “shoulder” spectrum, while the “D” points corresponds to a local minimum that tends to produce a “dip” spectrum. The larger letter indicates which minimum is the global minimum for a particular infall velocity.

The lower panels of figure 8 show the hill model variants infall velocities compared to the infall velocities in those same clouds. Once again we see that HILL5 does a good job of matching most of the infall velocities using the  $\text{HCO}^+$  ( $J = 1 \rightarrow 0$ ) line profile, but tends to break down at high velocities. Overall the HILL5 model fits to the  $\text{HCO}^+$  ( $J = 1 \rightarrow 0$ ) match the simulated infall velocities with an RMS error of  $0.08 \text{ km s}^{-1}$  over the full range of simulated infall velocities, however for infall velocities less than 1.5 times the velocity dispersion the RMS error is less than  $0.01 \text{ km s}^{-1}$ . The HILL5 infall velocity fits break down at an even lower infall velocity in the case of the  $\text{HCO}^+$  ( $J = 3 \rightarrow 2$ ) line, however the overall RMS error in the infall velocity fits for that transition are only  $0.07 \text{ km s}^{-1}$ . We believe this is because the contribution of the red component is so low in these cases. When the magnitude of the red component drops HILL5 does not produce a good profile fit (see the topmost spectrum of figure 6). We also believe that the HILL5 model does a poor job when the shoulder starts to disappear yielding a sloping asymmetric line such as the uppermost spectrum of figure 7. Once again the HILL6 model does a poor job at fitting low infall velocities. The HILL7 does a good job at fitting all the infall velocities in both line transitions, typically within  $0.03 \text{ km s}^{-1}$  of the modeled value. The error in the fit begins to increase, especially in the case of the  $\text{HCO}^+$  ( $J = 1 \rightarrow 0$ ) fit, as the infall velocity increases. This is due to the diminishing magnitude of the red-shifted component. As the blue-shifted component begins to dominate the HILL7 model fit, the seven parameters of the model begin to overdetermine the line profile, resulting in a range of solutions that fit equally well. In practice it is possible to avoid this by reducing the number of parameters and using the HILL6 model, however in most observed infall profiles the magnitudes of both the red and blue components are not as large as seen in the top panel of figure 6 (cf. Lee et al. 2001). In typical line profiles, such as those seen in this spherically symmetric infalling cloud, with a uniform infall velocity in the outer layers, the HILL5 does an excellent job at extracting the infall velocity, while the TWOLAYER6 does an adequate job for lines with a small red peak or narrow shoulder component.

### 4.3. Simulation C — Core Infall

We confine infall to the core ( $r < r_0$ ), and surround the infall region with a static envelope in Simulation C. The resulting  $\text{HCO}^+$  and  $\text{H}^{13}\text{CO}^+$  ( $J = 1 \rightarrow 0$ ) line profiles are shown in figure 10. The  $\text{HCO}^+$  and  $\text{H}^{13}\text{CO}^+$  ( $J = 3 \rightarrow 2$ ) line profiles are shown in figure 11. Once again modeled infall velocity, this time in the core, is increasing upwards. The bottom spectra are for no infall velocity, the middle spectra are for an infall velocity equal to the velocity dispersion of  $0.1 \text{ km s}^{-1}$ , and the top spectra are for an infall velocity of  $0.2 \text{ km s}^{-1}$ . The first thing we notice is that the  $\text{HCO}^+$  ( $J = 1 \rightarrow 0$ ) lines are not very blue-asymmetric.

Although the width increases as the infall velocity in the core increases, the infall asymmetry does not because the  $J = 1 \rightarrow 0$  transition is mostly sensitive to motions in the envelope. The emission from the core is mostly absorbed by the envelope because the optical depth in the  $J = 1 \rightarrow 0$  line is high. The  $\text{HCO}^+$  ( $J = 3 \rightarrow 2$ ) transition, which is more optically thin, does a better job of probing the motions in the core, and shows a greater degree of asymmetry as the infall velocity increases.

The low level of asymmetry in the  $J = 1 \rightarrow 0$  line results in a relatively poor fit to the infall velocity for both the two-layer model variants and the hill model variants. Figure 12 depicts the efficacy of the model variants at matching the simulated infall velocity in this simulation. The TWOLAYER5, TWOLAYER6, HILL5, and HILL7 all significantly underestimate the infall velocity from the  $\text{HCO}^+$  ( $J = 1 \rightarrow 0$ ) line profiles. This is not surprising as that transition is very thick and not very sensitive to the motions in the core, where the infall is occurring. The HILL5 fit tends to be consistently a factor of  $\sim 5$  lower than the simulated infall velocity. The situation is more encouraging when examining the thinner  $\text{HCO}^+$  ( $J = 3 \rightarrow 2$ ) line profile fits. The TWOLAYER5 model continues to significantly underestimate the infall velocity, but the TWOLAYER6 model matches the simulated infall velocity well for velocities between  $0.1 \text{ km s}^{-1}$  and to  $0.15 \text{ km s}^{-1}$ . Overall the RMS error on the infall velocity fits of the TWOLAYER6 model to the  $\text{HCO}^+$  ( $J = 3 \rightarrow 2$ ) lines is  $0.03 \text{ km s}^{-1}$ . The HILL5 model continues to underestimate the infall velocity from the  $\text{HCO}^+$  ( $J = 3 \rightarrow 2$ ) line, resulting in an RMS error on the fit infall velocity of  $0.07 \text{ km s}^{-1}$ . We believe this is due to the fact that the red peak quickly becomes a shoulder in this simulation, and the HILL5 model tends to do much better when fitting a distinct red peak. The HILL6 model overestimates the infall velocity, while the HILL7 model tends to do about as well as the TWOLAYER6 model at estimating the infall velocity when fitting the  $\text{HCO}^+$  ( $J = 3 \rightarrow 2$ ) lines in this simulation. Both the HILL7 model and the TWOLAYER6 model begin to underestimate the infall velocity for core infall velocities greater than approximately  $0.14 \text{ km s}^{-1}$ . At this point we run into the problem that the line profile is not becoming more asymmetric, just wider, due to the increasing velocities in the core.

#### 4.4. Simulation D — Dense Bonnor-Ebert Sphere

In our fourth simulation we choose a different density profile and a uniform velocity throughout the cloud. We specifically choose the Bonnor-Ebert fit to the density profile of B68 obtained by using extinction measurements of the background K giant population to produce an azimuthally averaged column density profile (Alves, Lada, & Lada 2001). We

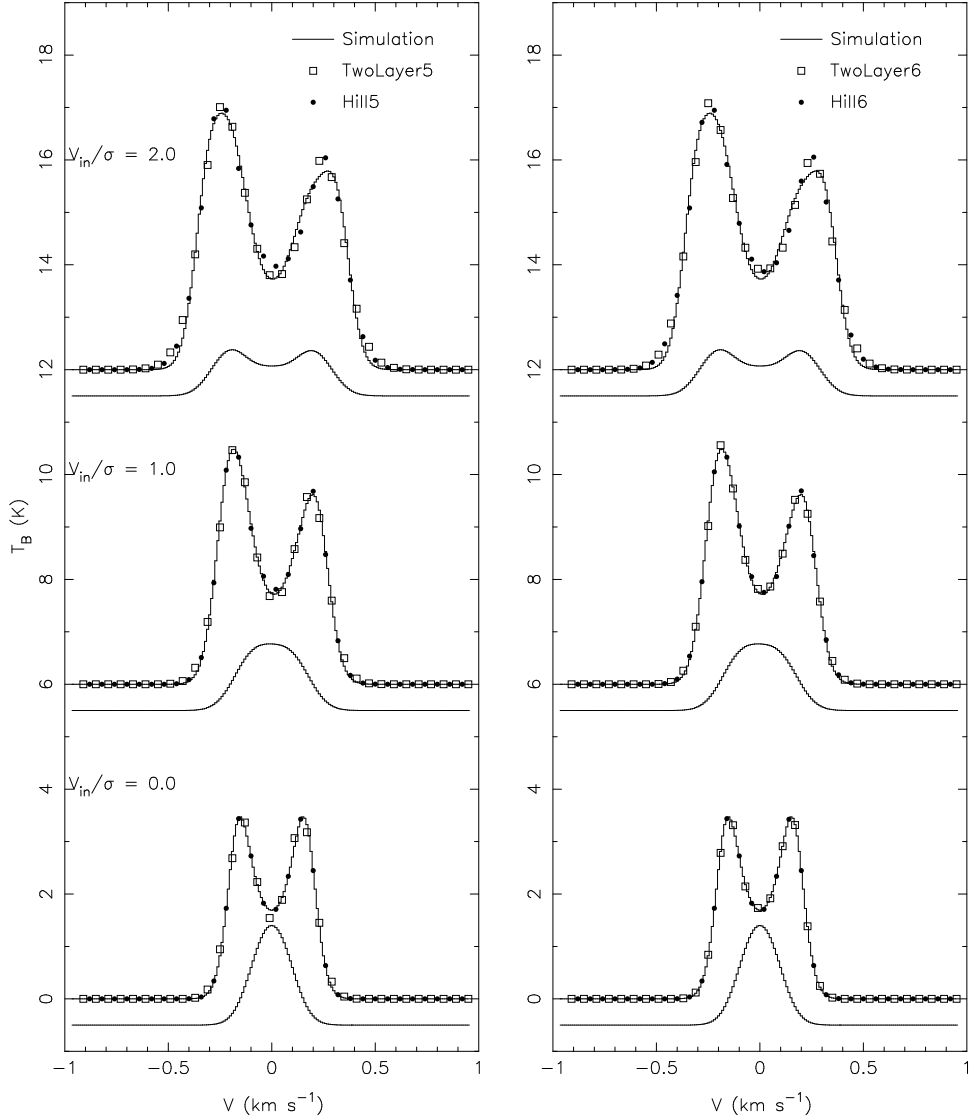


Fig. 10.— Monte Carlo simulated spectra (solid lines) of the  $\text{HCO}^+$  ( $J = 1 \rightarrow 0$ ) and  $\text{H}^{13}\text{CO}^+$  ( $J = 1 \rightarrow 0$ ) (multiplied by a factor of 5) emission from Simulation C (Core Infall). The infall velocity in the lowest set of spectra is  $0 \text{ km s}^{-1}$ , those in the middle are of a cloud infalling at  $0.1 \text{ km s}^{-1}$ , while those at the top are of a cloud infalling at  $0.2 \text{ km s}^{-1}$ . The analytic model fits are overlaid on each  $\text{HCO}^+$  spectrum. The open squares on the left indicate the TWOLAYER5 fits, while the filled circles are the HILL5 fits. On the right the open squares indicate the TWOLAYER6 fits, while the filled circles indicate the HILL6 fit.



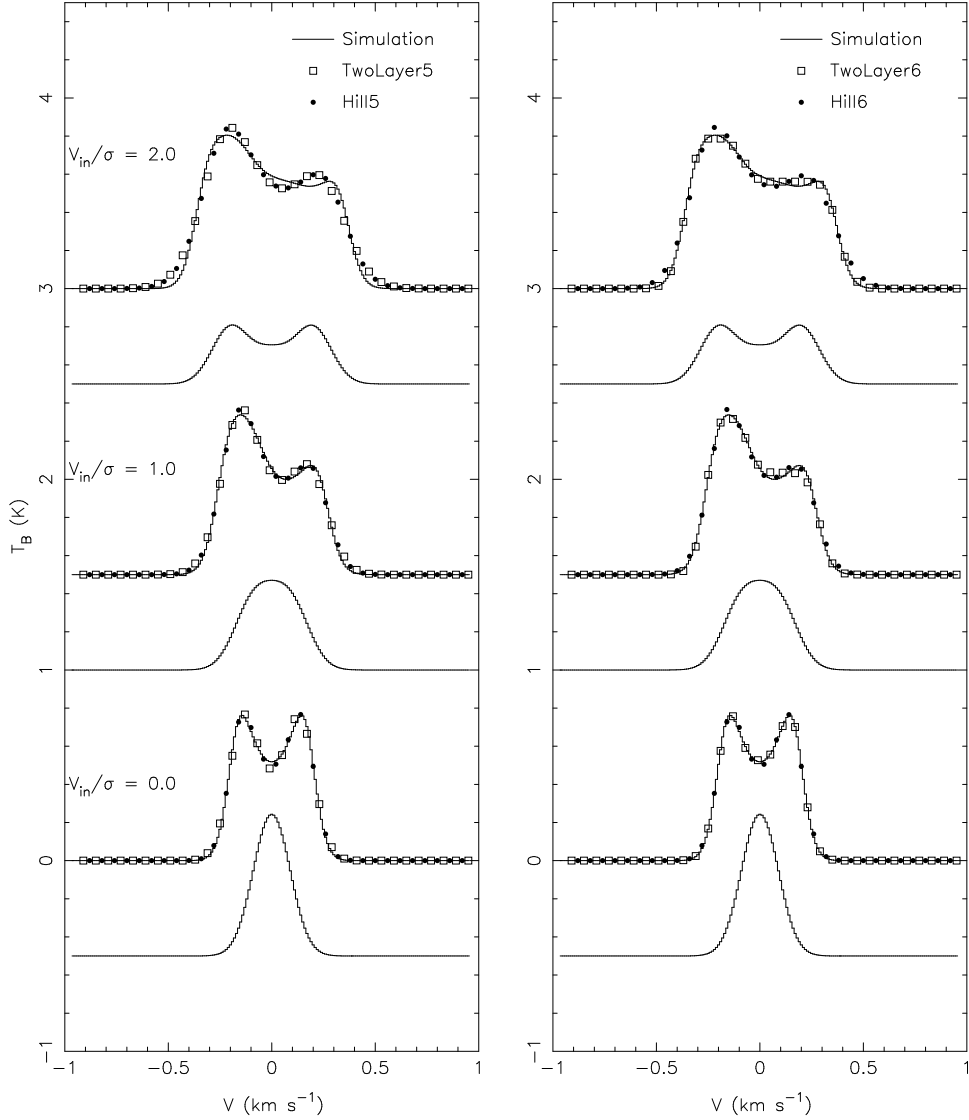


Fig. 11.— Monte Carlo simulated spectra (solid lines) of the  $\text{HCO}^+$  ( $J = 3 \rightarrow 2$ ) and  $\text{H}^{13}\text{CO}^+$  ( $J = 3 \rightarrow 2$ ) (multiplied by a factor of 40) emission from Simulation C (Core In-fall). The infall velocity in the lowest set of spectra is  $0 \text{ km s}^{-1}$ , those in the middle are of a cloud infalling at  $0.1 \text{ km s}^{-1}$ , while those at the top are of a cloud infalling at  $0.2 \text{ km s}^{-1}$ . The analytic model fits are overlaid on each  $\text{HCO}^+$  spectrum. The open squares on the left indicate the TWOLAYER5 fits, while the filled circles are the HILL5 fits. On the right the open squares indicate the TWOLAYER6 fits, while the filled circles indicate the HILL6 fit.

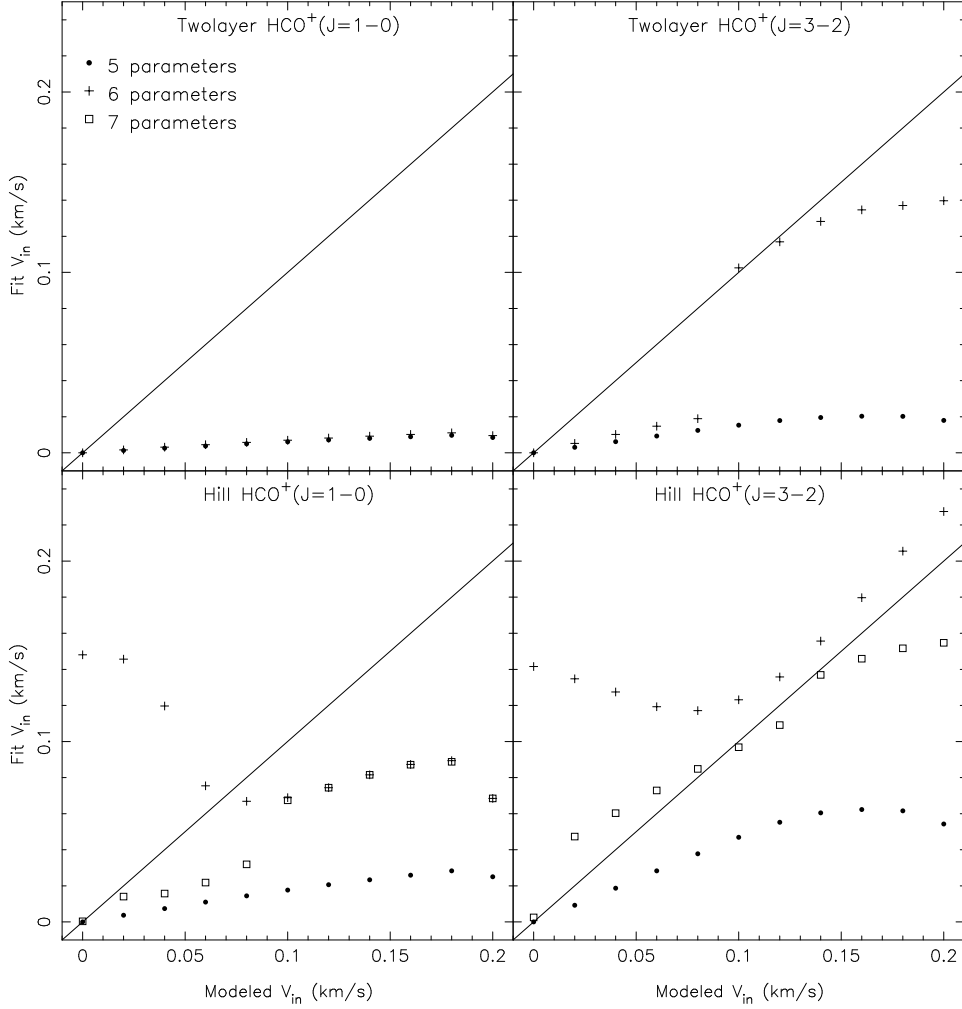


Fig. 12.— Infall velocity fits. The above figures indicate the infall velocities obtained by fitting TWOLAYER5, TWOLAYER6, HILL5, HILL6, and HILL7 models to the Monte Carlo simulated spectra in Simulation C (Core Infall). The left hand panels are the results of fitting the  $\text{HCO}^+$  ( $J = 1 \rightarrow 0$ ) spectra, and the right hand panels are the results of fitting the  $\text{HCO}^+$  ( $J = 3 \rightarrow 2$ ) spectra. The top two figures indicate the infall velocities obtained from the two-layer models. Below the two-layer results are the results of the hill models. The symbols indicate the number of free parameters, closed circles indicate the 5 free parameter models (TWOLAYER5 and HILL5). Crosses indicate the 6 free parameter models (TWOLAYER6 and HILL6). Open squares indicate the 7 free parameter model (HILL7). The TWOLAYER6 model often has two local minima, one of which is usually fit by the TWOLAYER5 model. We show the other local minimum when it is available in this plot.

calculate the Bonnor-Ebert density profile using the modified Lane-Emden equation

$$\frac{1}{\xi^2} \frac{d}{d\xi} \left( \xi^2 \frac{d\Psi}{d\xi} \right) = e^{-\Psi}, \quad (11)$$

where  $\xi = (r/a)\sqrt{4\pi G\rho_c}$  is the non-dimensional radial parameter,  $a$  is the isothermal sound speed,  $\rho_c$  is the volume density at the cloud center, and  $\Psi(\xi) = -\ln(\rho/\rho_c)$ . We split this second order differential equation in to two first order equations by using the variable substitutions suggested by Ballesteros-Paredes, Klessen, & Vázquez-Semadeni (2003) and integrate the equations numerically to derive the density profile. We use  $\xi_{\max} = 6.9$ , the free parameter derived by Alves et al. (2001) to be the best fit to the B68 cloud extinction observations. Di Francesco et al. (2002) find that the relative abundance of  $\text{HCO}^+$  to molecular hydrogen is less than  $1.4 \times 10^{-10}$ , which is significantly lower than the value of  $2 \times 10^{-9}$  which we have been using. Under such low abundances the  $\text{HCO}^+$  lines we would derive from radiative transfer calculations within this model cloud would be optically thin. Since optically thick lines are required for our analysis, we choose to maintain the  $\text{HCO}^+$  to molecular hydrogen relative abundance at  $2 \times 10^{-9}$  and only change the density profile in this simulation. We divide the spherical cloud into thirty equally spaced shells, the central shell has a molecular hydrogen density of  $2.6 \times 10^5 \text{ cm}^{-3}$ , while the outermost shell has a molecular hydrogen density of  $1.6 \times 10^4 \text{ cm}^{-3}$  and a maximum radius of  $1.87 \times 10^{17} \text{ cm}$  or 12,500 AU. We assume a constant kinetic temperature of 11 K throughout the cloud, as obtained by Lai et al. (2003) using  $\text{NH}_3$  (1,1) and (2,2) hyperfine line observations conducted at the DSN 34m telescope.

We assume a constant infall velocity throughout the cloud at all radii. We modeled 11 infall velocities ranging from 0 to twice the velocity dispersion, which we chose to be  $0.12 \text{ km s}^{-1}$ . We base our choice of the velocity dispersion on the  $\text{N}_2\text{H}^+$  ( $J = 1 \rightarrow 0$ ) line width in B68 reported by Caselli et al. (2002a).  $\text{HCO}^+$  ( $J = 1 \rightarrow 0$ ) and  $\text{H}^{13}\text{CO}^+$  ( $J = 1 \rightarrow 0$ ) spectra from this simulation are shown in figure 13. As in previous simulations we choose a representative sample of three spectra in the direction of the cloud center at different infall velocities. In this case the infall velocities are  $0 \text{ km s}^{-1}$ ,  $0.12 \text{ km s}^{-1}$ , and  $0.24 \text{ km s}^{-1}$ . On the left side of figure 13 the best fit TWOLAYER5 and HILL5 models are shown, while on the right side the best fit TWOLAYER6 and HILL6 models are shown. The first thing to note is that the  $\text{H}^{13}\text{CO}^+$  lines are slightly asymmetric, similar to  $\text{H}^{13}\text{CO}^+$  ( $J = 1 \rightarrow 0$ ),  $\text{HC}^{18}\text{O}^+$  ( $J = 1 \rightarrow 0$ ), and  $\text{D}^{13}\text{CO}^+$  ( $J = 2 \rightarrow 1$ ) observations of L1544 seen in figure 1 of Caselli et al. (2002b). This is as a result of self-absorption, because although the  $\text{H}^{13}\text{CO}^+$  molecule has an abundance 64 times lower than that of  $\text{HCO}^+$ , it is not so low that it is optically thin. It is important to be aware of that asymmetry may arise in less abundant species, however the degree of asymmetry is indeed less than the asymmetry of the more abundant  $\text{HCO}^+$  molecule. As in previous simulations, the line profiles generated by the analytic models reproduce the Monte Carlo generated profiles very well. Similar

results for the  $\text{HCO}^+$  ( $J = 3 \rightarrow 2$ ) and  $\text{H}^{13}\text{CO}^+$  ( $J = 3 \rightarrow 2$ ) lines are shown in figure 14. The  $\text{H}^{13}\text{CO}^+$  lines are more symmetric in this case as there is less optical depth along the line of sight.

We compare the infall velocities in this simulation with those obtained by fitting the line profiles with our analytic models in figure 15. As in previous sections we present the fits to the  $\text{HCO}^+$  ( $J = 1 \rightarrow 0$ ) line profiles on the left panels of the figure, and those to the  $\text{HCO}^+$  ( $J = 3 \rightarrow 2$ ) line profiles on the right panels of the figure. The upper panels refer to the two-layer model fits, while the lower panels refer to the hill model fits. Neither of the two-layer models reproduce the simulated infall velocity across the entire range of infall velocities we tested. The RMS systematic error in the TWOLAYER6 model fits of  $\text{HCO}^+$  ( $J = 1 \rightarrow 0$ ) is  $0.03 \text{ km s}^{-1}$ , and  $0.04 \text{ km s}^{-1}$  with respect to the  $\text{HCO}^+$  ( $J = 3 \rightarrow 2$ ) fits. The HILL5 model does a better job at estimating the infall velocity in the simulated clouds. The RMS systematic error in the HILL5 estimates of the infall velocity based on the  $\text{HCO}^+$  ( $J = 1 \rightarrow 0$ ) profile fits is  $0.03 \text{ km s}^{-1}$ , while the RMS systematic error based on the  $\text{HCO}^+$  ( $J = 3 \rightarrow 2$ ) profile fits is  $0.01 \text{ km s}^{-1}$ . As we have seen in previous simulations the TWOLAYER6 model yields a closed fit to the infall velocity at higher infall velocities. The HILL5 model provides a fairly good fit for all infall velocities. These results are similar to the results obtained in Simulation A (Constant Infall), which is the other simulation in which infall was constant at all radii. This is reassuring as the central densities in these two simulations differ by a factor of 4 and they have different radial density profiles. This suggests that these analytic models may be able to predict infall velocities from optically thick line profiles for a wide range of densities and radial density profiles in star forming clouds.

#### 4.5. Error Analysis

There are two components to the error in any fit of a model to data. The first, systematic error, is error which arise in the model’s description of the data. It is due to the fact that the model may not correctly describe the nature of the observed region. The second component is random error, which arises from noise in the observation. Although random error can be reduced over time or with better instrumentation, usually up to some limit, it is always a factor in any observation, and in fitting a model to those observations. In the preceding sections we examined how well our analytic radiative transfer models fit synthetic noiseless spectra. From this we found systematic errors due to the models shown in figures 5 and 8. In order to investigate the behavior of the fits in the presence of random error we decided to add noise to the spectra.

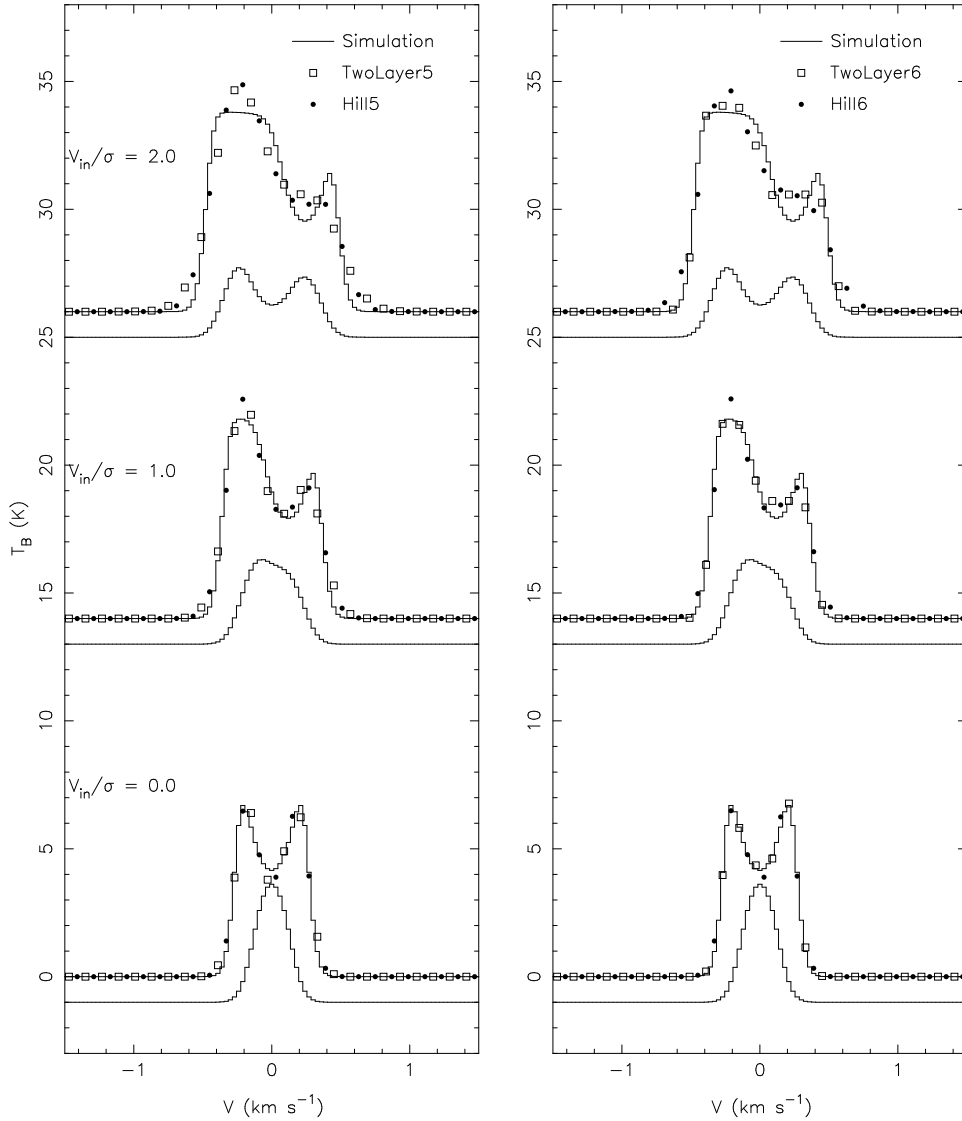


Fig. 13.— Monte Carlo simulated spectra (solid lines) of the  $\text{HCO}^+$  ( $J = 1 \rightarrow 0$ ) and  $\text{H}^{13}\text{CO}^+$  ( $J = 1 \rightarrow 0$ ) (multiplied by a factor of 2) emission from Simulation D (Dense Bonnor-Ebert Sphere). The infall velocity in the lowest set of spectra is  $0 \text{ km s}^{-1}$ , those in the middle are of a cloud infalling at  $0.12 \text{ km s}^{-1}$ , while those at the top are of a cloud infalling at  $0.24 \text{ km s}^{-1}$ . The analytic model fits are overlaid on each  $\text{HCO}^+$  spectrum. The open squares on the left indicate the TWOLAYER5 fits, while the filled circles are the HILL5 fits. On the right the open squares indicate the TWOLAYER6 fits, while the filled circles indicate the HILL6 fit.

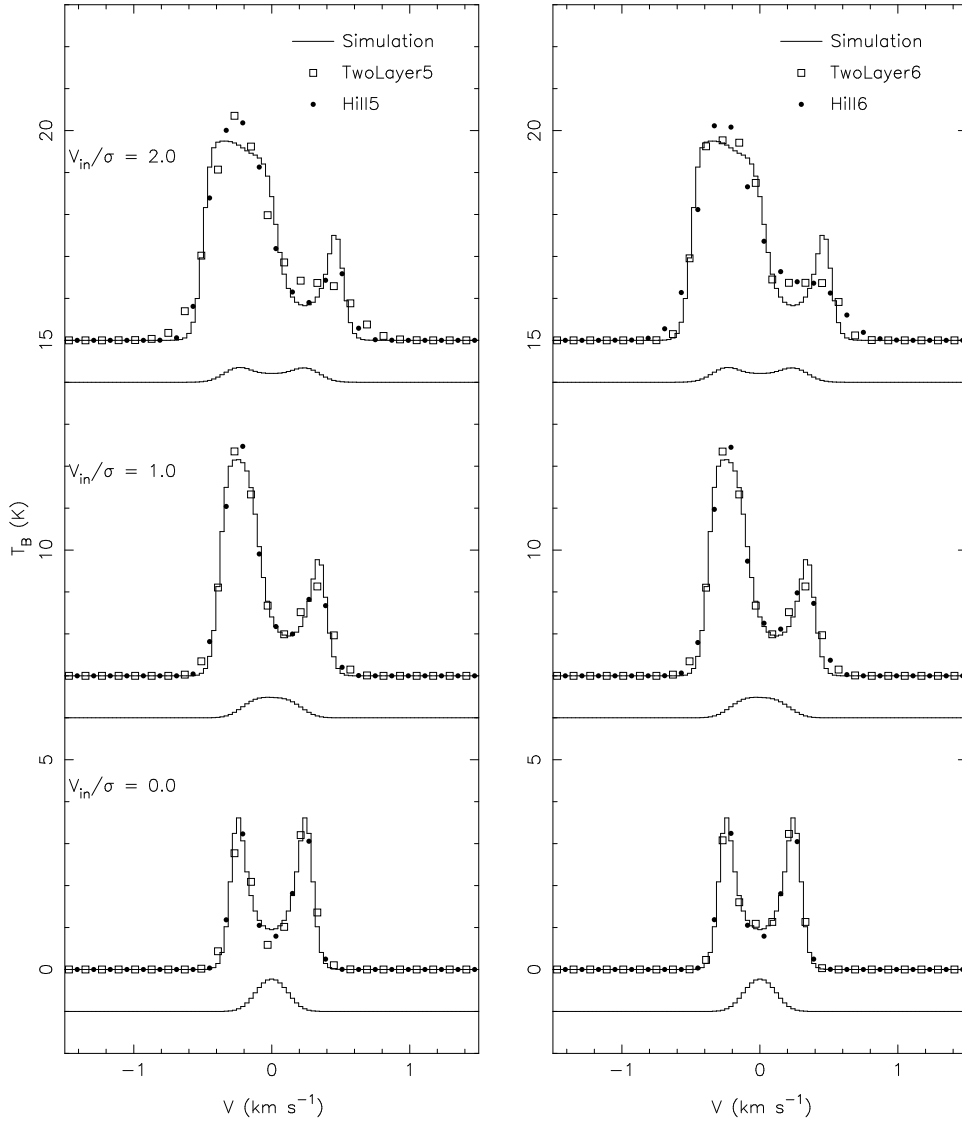


Fig. 14.— Monte Carlo simulated spectra (solid lines) of the  $\text{HCO}^+$  ( $J = 3 \rightarrow 2$ ) and  $\text{H}^{13}\text{CO}^+$  ( $J = 3 \rightarrow 2$ ) (multiplied by a factor of 2) emission from Simulation D (Dense Bonnor-Ebert Sphere). The infall velocity in the lowest set of spectra is  $0 \text{ km s}^{-1}$ , those in the middle are of a cloud infalling at  $0.12 \text{ km s}^{-1}$ , while those at the top are of a cloud infalling at  $0.24 \text{ km s}^{-1}$ . The analytic model fits are overlaid on each  $\text{HCO}^+$  spectrum. The open squares on the left indicate the TWOLAYER5 fits, while the filled circles are the HILL5 fits. On the right the open squares indicate the TWOLAYER6 fits, while the filled circles indicate the HILL6 fit.

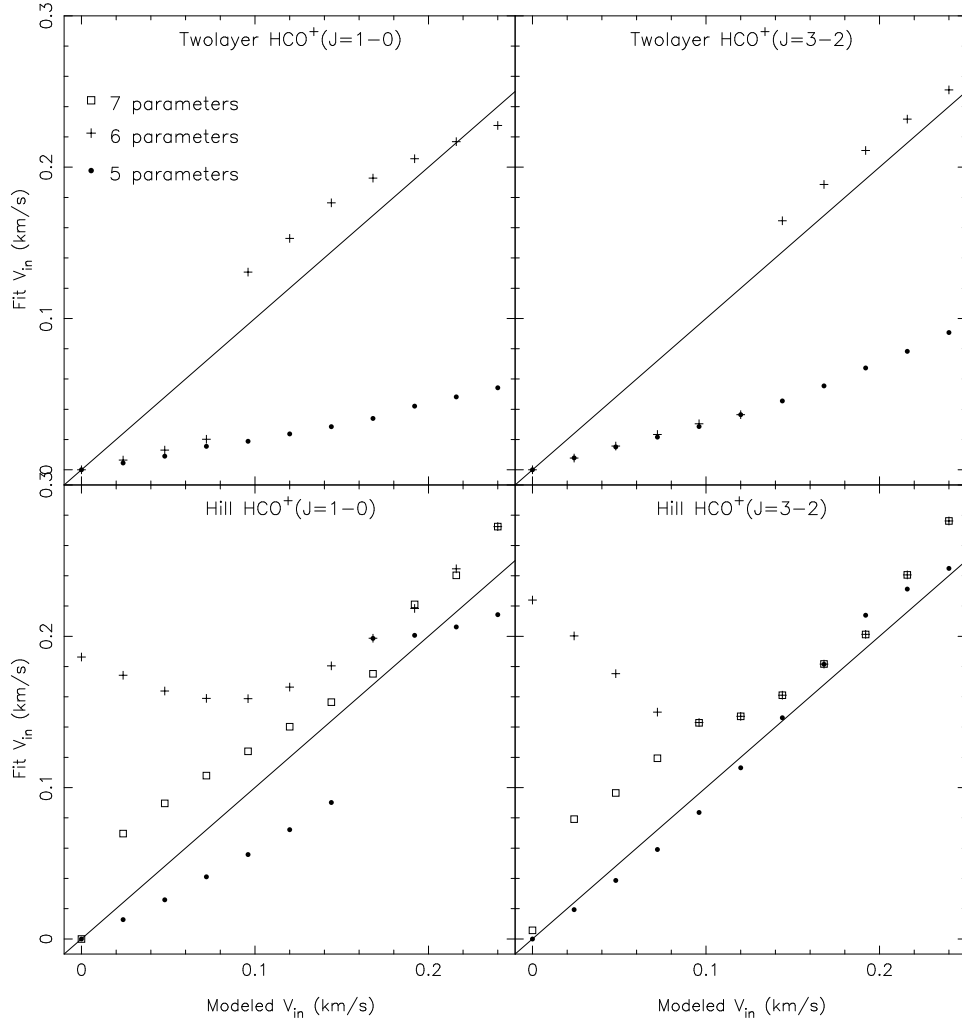


Fig. 15.— Infall velocity fits. The above figures indicate the infall velocities obtained by fitting TWOLAYER5, TWOLAYER6, HILL5, HILL6, and HILL7 models to the Monte Carlo simulated spectra in Simulation D (Dense Bonnor-Ebert Sphere). The left hand panels are the results of fitting the  $\text{HCO}^+$  ( $J = 1 \rightarrow 0$ ) spectra, and the right hand panels are the results of fitting the  $\text{HCO}^+$  ( $J = 3 \rightarrow 2$ ) spectra. The top two figures indicate the infall velocities obtained from the two-layer models. Below the two-layer results are the results of the hill models. The symbols indicate the number of free parameters, closed circles indicate the 5 free parameter models (TWOLAYER5 and HILL5). Crosses indicate the 6 free parameter models (TWOLAYER6 and HILL6). Open squares indicate the 7 free parameter model (HILL7). The TWOLAYER6 model often has two local minima, one of which is usually fit by the TWOLAYER5 model. We show the global minimum in this plot.

Barranco & Goodman (1998) have derived analytic expressions for the contribution of random error in a spectrum to the three parameters of a Gaussian fit based upon the work of Landman et al. (1982). They find that the random error in the line of sight velocity and in the velocity dispersion of a Gaussian fit are the same and equal to

$$\sigma_{v_{\text{LSR}}} = \sigma_{\sigma} = 1.06 (\delta_v \sigma)^{1/2} \frac{\sigma_{\text{RMS}}}{T_A^*}, \quad (12)$$

where  $v_{\text{LSR}}$  is the line of sight velocity of the Gaussian,  $\sigma$  is the velocity dispersion of the Gaussian,  $\delta_v$  is the width of the spectral channels,  $T_A^*$  is the peak intensity of the Gaussian line profile, and  $\sigma_{\text{RMS}}$  is the RMS noise level in the spectrum. Unfortunately deriving expressions for the random error in the parameters of the two-layer or hill models is more difficult. We therefore use a bootstrap method to investigate the errors in the parameters of these models. We generate a noiseless synthetic spectrum from one of the above simulations, add random noise to it, and then perform the analytic radiative transfer model fits. We do this 100 times with different random noise of the same RMS value in order to record the variance of each model parameter. Assuming the errors are normally distributed, we find that the random error in each parameter is merely the square root of the variance in that parameter.

We initially tested the method on Gaussian line fits, whose random errors should follow the expression in equation 12. Figure 16 shows our resulting error determinations for different RMS noise values (filled circles) versus the expected value (solid line). We express the RMS noise in terms of the signal to noise ratio on the lower axis, and also in terms of the integration time it would take to achieve a given RMS for a telescope with a system temperature of 200 K and a main beam efficiency of 0.5 when observing a Gaussian line with a peak brightness temperature of 5 K, along the top axis. We also use a channel width of  $0.04 \text{ km s}^{-1}$  in this case, less than the input  $0.1 \text{ km s}^{-1}$  velocity dispersion of the Gaussian line and typical of current spectrometers. The bootstrap estimates are a good fit to equation 12, with minimal scatter due to the random nature of the technique. This test indicates that the bootstrap method is a robust estimator of the random error in the parameters of the Gaussian fit and should be a robust estimator of the random error in the parameters of the analytic radiative transfer model fits.

We apply the bootstrap method to the  $\text{HCO}^+$  ( $J = 1 \rightarrow 0$ ) line profiles of Simulation A (Constant Infall) shown in figure 3. Figure 17 summarizes our findings for the random errors in the velocity dispersion, infall velocity, and line of sight velocity parameters of the HILL5 model. The closed circles indicate the error in parameters as a function of integration time for a spectral resolution of  $0.04 \text{ km s}^{-1}$ , while the open circles are those for a spectral resolution of  $0.16 \text{ km s}^{-1}$ . The error increases with the lower spectral resolution because the self-absorption feature starts to be resolved out at that resolution. The cross in the center of each panel indicates the average systematic error obtained from the fits on figure 5. The



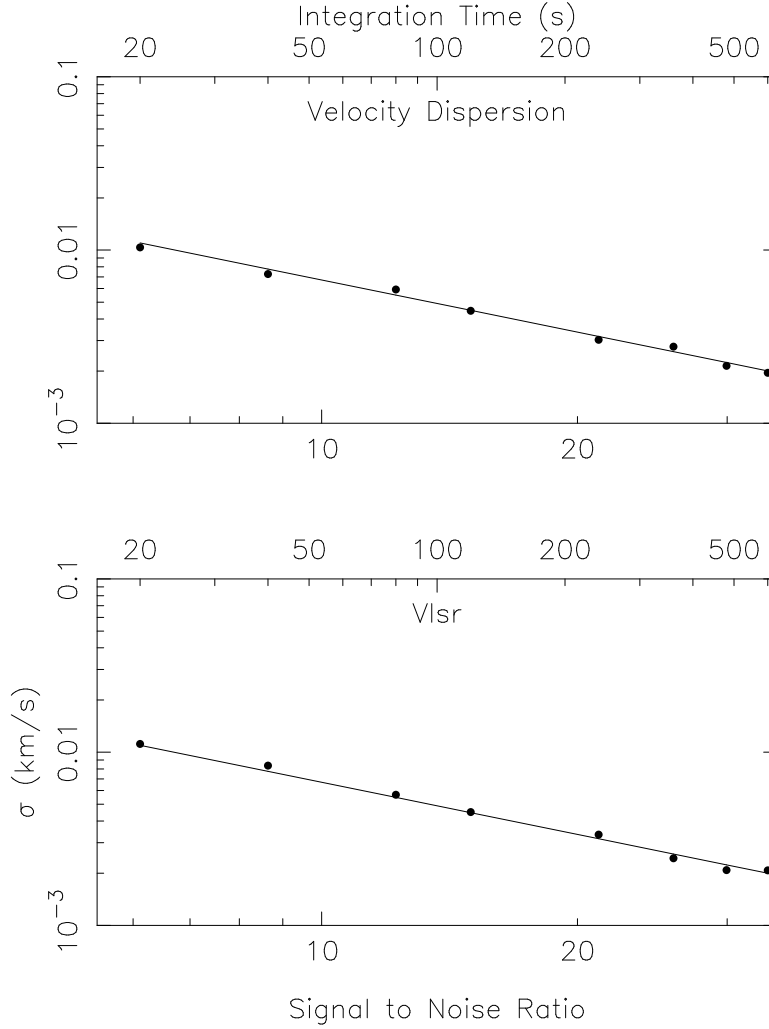


Fig. 16.— Random errors in a Gaussian fit to the velocity dispersion and line of sight velocity. We estimated errors to a Gaussian fit using a bootstrap method and compared those errors to the theoretically predicted errors in a Gaussian fit to a noise spectrum derived by Barranco & Goodman (1998). The filled circles are our bootstrap estimates for several different RMS noise levels. We use signal to noise ratios in the lower x-axis. We also convert the RMS to an integration time assuming a velocity resolution of  $0.04 \text{ km s}^{-1}$  in the spectrum, a main beam efficiency of 0.5 and a system temperature of 200 K and place that integration time estimate on the upper x-axis. The Gaussian we fit in the example has a peak line temperature of 5.01 K and a velocity dispersion of  $0.1 \text{ km s}^{-1}$ .

average systematic error in the velocity dispersion is  $0.008 \text{ km s}^{-1}$ , the average systematic error in the infall velocity is  $0.009 \text{ km s}^{-1}$ , while the average systematic error in the line of sight velocity is  $0.005 \text{ km s}^{-1}$ . The solid line in both the velocity dispersion panel and the line of sight velocity panel are the Gaussian errors from figure 16. Unsurprisingly the errors in the hill model parameters are greater than those in the Gaussian fit, which has fewer free parameters of the HILL5 model, however they tend to follow a similar power law trend with increasing integration times. What we can see from this plot is that it is possible to be dominated by the systematic errors of the hill model after a reasonable amount of integration time on a typical millimeter radio telescope. For spectral resolutions adequate to observe the line shape, the velocity dispersion random error drops below the systematic level after less than 30 seconds of integration, while the line of sight velocity is well determined after less than two minutes. Getting to a point where the systematic errors in the infall velocity dominate over the random errors takes the longest amount of time, but only about 10 minutes for a line whose brightness temperature is approximately 5 K. This means that generally the infall velocity is as well determined as it can get by the hill model when the signal to noise ratio is greater than  $\sim 30$ . We assume, based on our experience with gaussian line fitting that maintaining a similar signal to noise ratio in lines of differing peak intensities should yield similar errors. This implies an integration time of 30 minutes for a line whose brightness temperature is approximately 3 K, and 250 minutes for a line whose brightness temperature is approximately 1 K. This means the observations required to obtain the required signal to noise can take a prohibitively long time for weak asymmetric line profiles.

#### 4.6. Depletion and Beam Smoothing

Depletion in high density regions of a molecular cloud core is a significant effect in observed infall regions. Many observations of CO, CS, and HCO<sup>+</sup> in dense cores show a ring distribution thought to result from an abundance drop in the gas phase due to freeze out of these molecules onto grains (Kuiper et al. 1996; Willacy et al. 1998; Kramer et al. 1999; Alves et al. 1999; Caselli et al. 1999; Bergin et al. 2001; Jessop & Ward-Thompson 2001; Bacmann et al. 2002; Tafalla et al. 2002, 2004). We have added depletion in some cases to perform an investigation of the efficacy of the analytic models at estimating the infall velocity as depletion increases. We adopt the formalism of Tafalla et al. (2002) and set the abundance of HCO<sup>+</sup> to vary exponentially with the density,

$$X(r) = X_0 \exp[-n(r)/n_d], \tag{13}$$

where  $X(r)$  is the abundance of HCO<sup>+</sup> as a function of cloud radius,  $X_0$  is the HCO<sup>+</sup> abundance in the low density limit ( $2 \times 10^{-9}$ ),  $n(r)$  is the density of molecular hydrogen as a

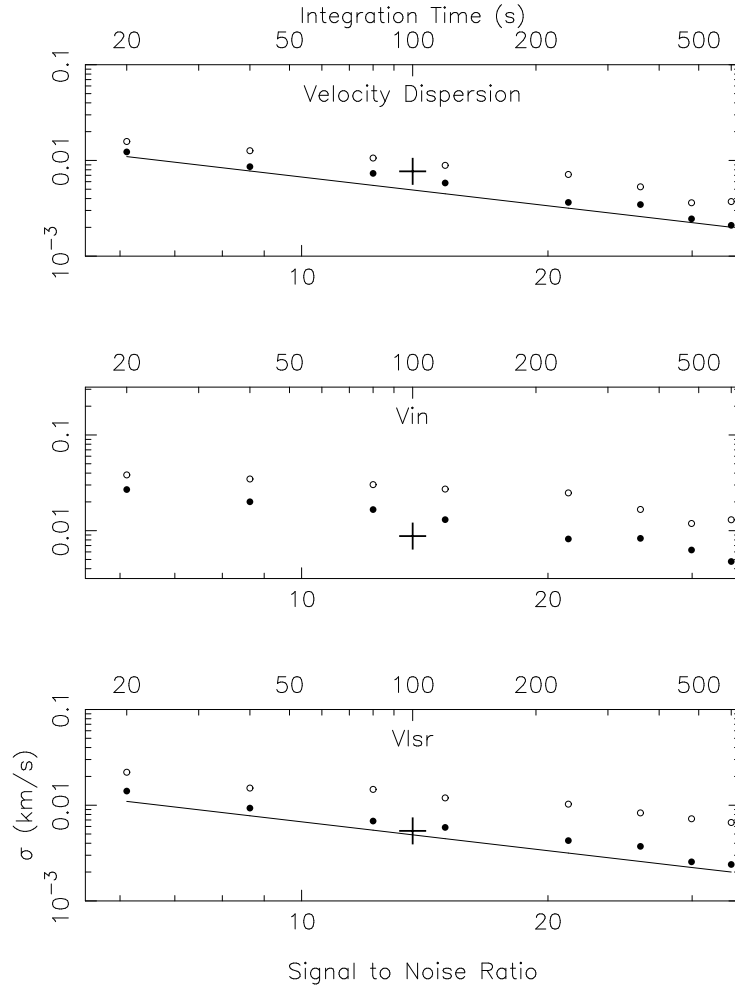


Fig. 17.— Systematic and random errors associated with the HILL5 model. We measured the average systematic error in the dispersion velocity, infall velocity, and line of sight velocity relative to our input models and plot them above as the large crosses. We then added noise to simulate integration times between 20 seconds and 600 seconds with velocity resolutions of  $0.04 \text{ km s}^{-1}$  (filled circles) and  $0.16 \text{ km s}^{-1}$  (open circles), and use the bootstrap method to measure the random errors in those same parameters. The upper x-axis indicates these integration times. The lower x-axis has a measurement of the signal to noise ratio for the  $0.04 \text{ km s}^{-1}$  resolution case. From this it is possible to estimate the signal to noise ratio required in order to have the random error drop below the systematic error for a given observation. We find that signal to noise ratios greater than 30 are required, using the  $\text{HCO}^+ (J = 1 \rightarrow 0)$  lines modeled in figure 3 as a template. The solid line indicates the theoretical Gaussian errors for dispersion velocity and line of sight velocity as a function of time under the same assumptions.

function of cloud radius, and  $n_d$  is the density at which the abundance drops by a factor of  $e$ . We included depletion in the Simulation A (Constant Infall) case where  $v_{\text{in}} = 0.1 \text{ km s}^{-1}$  for  $n_d = 10^6, 10^{5.5}, 10^5, 10^{4.5}, 10^4, 10^{3.5}$ , and  $10^3 \text{ cm}^{-3}$ . We found for the HILL5 model the fit infall velocity changed by less than one hundredth of a kilometer per second down to an  $n_d$  of  $10^4 \text{ cm}^{-3}$  for the  $\text{HCO}^+$  ( $J = 1 \rightarrow 0$ ) line and  $10^5$  for the  $\text{HCO}^+$  ( $J = 3 \rightarrow 2$ ) line. Figure 18 illustrates that in each of these cases that level of depletion corresponds to a change in the line profile from a two-peaked self-absorbed profile to a “shoulder” profile. Severe depletion, beyond the levels reported in figure 18 tends to result in a line too weak to be observed. Based on this simulation, we infer that moderate levels of depletion which does not render the line profile symmetric or unobservable has only a small effect on the HILL5 model’s infall velocity determinations.

Another important observational effect is smoothing by a telescope beam. Our simulated line profiles were generated by integrating along a pencil beam through the center of a simulated cloud. We have generated 2 dimensional grids of pencil beam integrations of our simulated clouds and can convolve them to produce a simulated Gaussian telescope beam. We begin by projecting the cloud on the sky plane at a distance of 140 pc, so that a beam of  $60''$  is equal to a distance of about 0.04 pc in the cloud. We then convolved two cases from Simulation A (Constant Infall), where  $v_{\text{in}} = 0.1$  and  $0.2 \text{ km s}^{-1}$ , to generate beam sizes of  $20''$  (0.014 pc),  $40''$  (0.027 pc), and  $60''$  (0.041 pc) in the  $\text{HCO}^+$  ( $J = 1 \rightarrow 0$ ) and  $\text{H}^{13}\text{CO}^+$  ( $J = 1 \rightarrow 0$ ) lines. The resulting beam-smoothed line profile seen toward the center of each simulated clouds is shown in figure 19. From the left column of figure 19 we see that beam smoothing has a similar effect to depleting the core. This is not surprising as both depletion and beam smoothing tend to increase the relative contribution of emission from the envelope of the molecular cloud. Our investigation indicates that the infall speed is well fit in cases where the beam width is less than or equal to the core diameter ( $10^{17} \text{ cm}$  in our simulation), however this is dependent on both the density structure and velocity structure of the molecular cloud. In practical terms, a higher resolution probes a smaller region which may have a large infall velocity and therefore a more asymmetric line.

## 5. Applying the Analytic Models

As a final exercise we have applied the HILL5 model to a high signal to noise line profile. We have learned from the simulations that the HILL5 model is the most robust model for determining the infall velocity of a molecular cloud from the line profile for a majority of line profile shapes. In particular the HILL5 model yields a good fit when the line profile has distinct blue-shifted and red-shifted peaks with a self-absorption minimum between them.

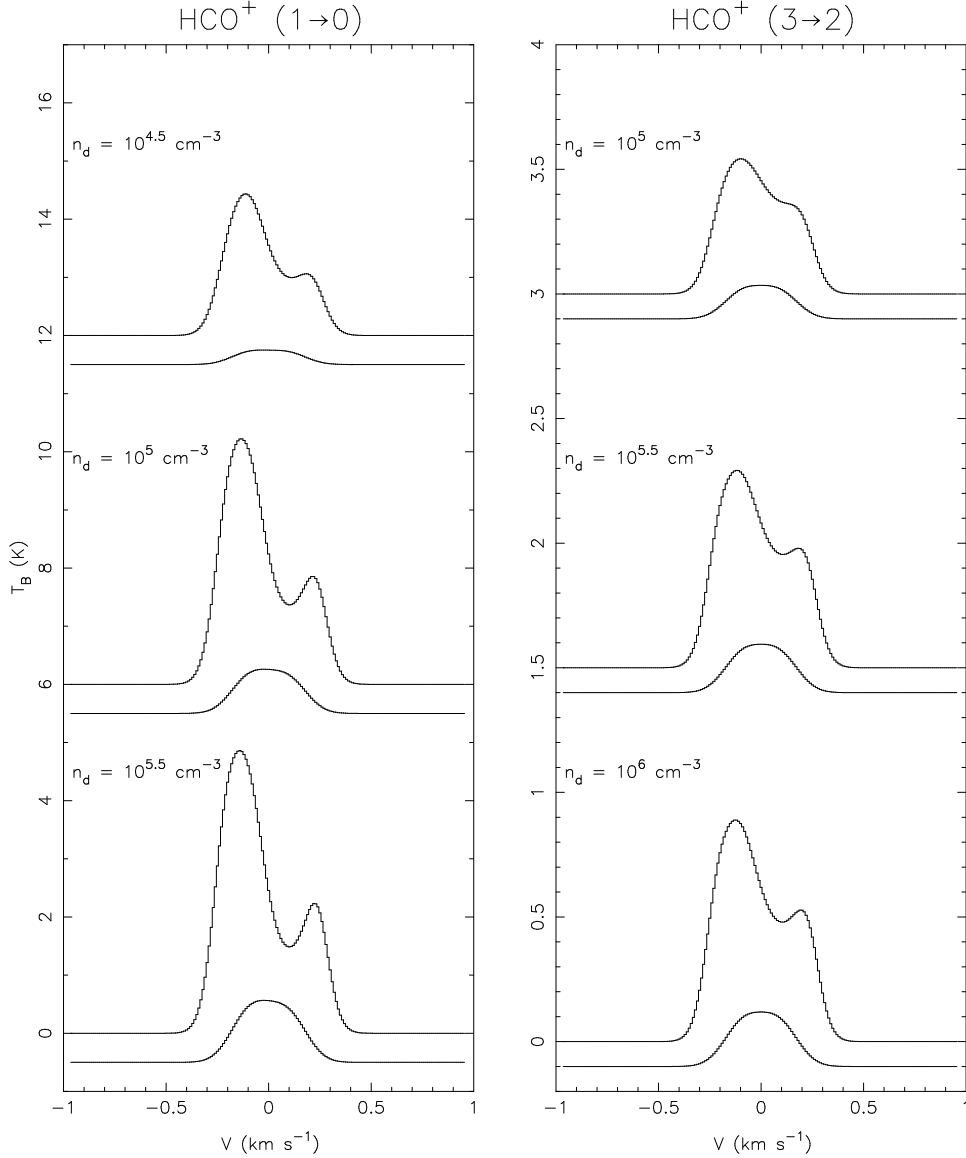


Fig. 18.— The effect of depletion on the HCO<sup>+</sup> and H<sup>13</sup>CO<sup>+</sup> ( $J = 1 \rightarrow 0$ ) (left) as well as the HCO<sup>+</sup> and H<sup>13</sup>CO<sup>+</sup> ( $J = 3 \rightarrow 2$ ) (right) line shapes. The depletion increases as the depletion density ( $n_d$ ) drops. In each column we highlight the range of depletions in which the transition remains bright ( $T_r > \sim 1$  K). In most cases the HILL5 model continues to provide a good fit to the infall velocity. The only exception is the upper-most set of spectra in which the HILL5 model is not applicable according to the prescription given in §5 as the dip between the peaks is not sufficiently deep. The H<sup>13</sup>CO<sup>+</sup> ( $J = 1 \rightarrow 0$ ) spectra have been multiplied by a factor of 5, and the H<sup>13</sup>CO<sup>+</sup> ( $J = 3 \rightarrow 2$ ) spectra have been multiplied by a factor of 20.

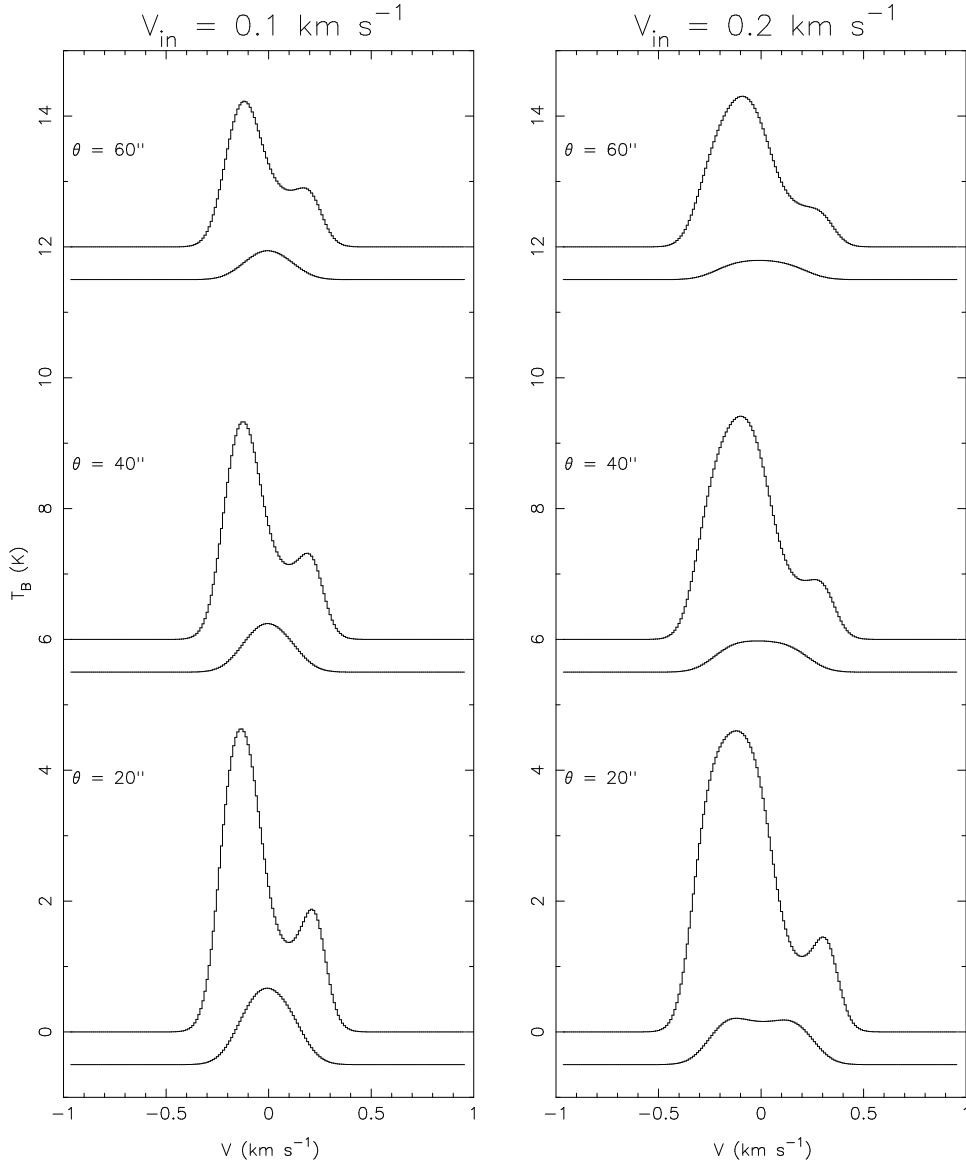


Fig. 19.— The effect of beam size of the  $\text{HCO}^+$  ( $J = 1 \rightarrow 0$ ) and  $\text{H}^{13}\text{CO}^+$  ( $J = 1 \rightarrow 0$ ) line profiles for Simulation A (Constant Infall) clouds with infall velocities of 0.1 and 0.2  $\text{km s}^{-1}$ . The simulated cloud is placed at a distance of 140 pc from the observer, typical of the nearest starless cores, and convolved with various beam sizes typical of current millimeter telescopes. The lowest spectra represent a beam size of 20'', the middle spectra represent a beam size of 40'', while the uppermost spectra represent a beam size of 60''. The left panel is a simulation of an infall velocity of 0.1  $\text{km s}^{-1}$  and the right panel is a simulation of an infall velocity of 0.2  $\text{km s}^{-1}$ . The  $\text{H}^{13}\text{CO}^+$  ( $J = 1 \rightarrow 0$ ) spectra have been multiplied by a factor of 5.

For line profiles with this shape, in simulations A and D, which had the same infall speed at all radii, the RMS error of the HILL5 infall velocity determination is  $0.01 \text{ km s}^{-1}$ , better than the overall RMS error in these simulations of  $0.02 \text{ km s}^{-1}$ . We recommend using the HILL5 model to derive infall velocities from asymmetric molecular line profiles.

In some cases there is little or no red-shifted peak, but merely a shoulder on the red side of the line profile. These cases tend to occur when the infall velocity is greater than the velocity dispersion. In Simulation A (Constant Infall) and Simulation C (Core Infall) red-shoulder profiles occur in the  $\text{HCO}^+$  ( $J = 3 \rightarrow 2$ ) transition for simulated infall velocities greater than  $0.1 \text{ km s}^{-1}$ , in Simulation B (Envelope Infall) red-shoulder profiles occur in both the transitions for infall velocities greater than  $0.1 \text{ km s}^{-1}$ , while in Simulation D (Dense Bonnor-Ebert Sphere) red-shoulder profiles never occur for all the infall velocities in our simulations. In these “shoulder” spectra the TWOLAYER6 model gives a comparable infall velocity estimate to the HILL5 model. We note that in Simulation C, where the TWOLAYER6 model performs better than the HILL5 model the red-shoulder model, lines tend to be weak ( $< 1 \text{ K}$ ). When using the TWOLAYER6 model it is important to choose the local minimum (which should also be the global minimum in these cases) that corresponds to the “shoulder” solution set. One can verify that the “shoulder” solution has been found by examining the best fit excitation temperature of the front layer, which should be greater than the background temperature. If the front layer excitation temperature is equal to the background temperature then it is likely that the one has found the “dip” solution which is usually never a good fit to the infall velocity.

Why is the HILL5 model good at finding the infall velocity of most clouds, while the TWOLAYER6 model is successful only on spectra with an asymmetric shoulder? The key to understanding this lies in how well each model matches the excitation conditions along the line of sight at each Doppler velocity. In figure 2 we presented cases in which both the HILL5 and TWOLAYER6 models match the excitation profile of the simulation quite well for  $\tau < 3$  at the line center velocity. Although the figure depicts only one Doppler velocity, the match continues to hold over the entire line profile. The resulting infall velocities derived from these models closely match the infall velocities in the simulated contracting cloud. In cases where the infall velocities derived from the analytic models do not match the infall velocities in the simulated clouds, the modeled excitation temperature profiles as a function of optical depth along the line of sight derived from the spectral line fits do not match the simulated excitation temperature profiles. Even in cases where the spectral line match is quite good, if the excitation conditions are not well matched then all the physical parameters, including the infall velocity, will not match the parameters of the simulated or observed cloud.

We find that the HILL5 model tends to reproduce the excitation temperature profile

as a function of optical depth quite well for a wide range of infall velocities. The reason that this is true is that the excitation conditions in a cloud do tend to rise as a function of optical depth over the first couple of optical depths, until the excitation temperature reaches the kinetic temperature of the core or begins dropping again as the density drops. In all of our simulations a linear fit to the rising excitation temperature, starting with an excitation temperature equal to the background temperature, is a good approximation of the actual excitation temperature profile at all Doppler velocities. As a result the HILL5 model is usually sensitive to the physical conditions of the collapsing cloud and yields a good estimate of the infall velocity if the cloud radii which comprise the first few optical depths of the line profile are infalling. For this reason we recommend using the HILL5 model. Our simulations and error analysis suggest that the line profile should have a peak brightness temperature greater than 1 K and a signal to noise ratio greater than 30. The line profile must also have a well defined dip or shoulder which must be resolved by the spectrometer resolution. If these conditions are met the HILL5 model can be expected to provide an estimate of the infall velocity with an accuracy of  $0.02 \text{ km s}^{-1}$ . Our simulations suggest the accuracy for dip profiles alone is  $0.01 \text{ km s}^{-1}$ .

The TWOLAYER6 model tends to reproduce the excitation temperature profile as a function of optical depth well only for higher infall velocities which tend to produce spectral lines that are very asymmetric or have well defined red shoulders. In these cases it may be tempting to use the TWOLAYER6 method to derive the infall velocity, however there are several caveats which one must take in to account. In cases with low infall velocities or more symmetric line profiles the excitation temperature of the front layer is often low (at or near the cosmic microwave background temperature) while that of the rear layers is often much higher than the maximum excitation temperature in the cloud, even in cases where the TWOLAYER6 model produces a good fit to the emerging line profiles. In these cases the infall velocities as other physical conditions derived from the TWOLAYER6 model do not match the conditions in the simulated cloud. The reason this occurs is that there is a certain amount of degeneracy in reproducing a symmetric or nearly symmetric line profile with the TWOLAYER6 model. A very high excitation temperature region behind a very low excitation temperature region produces the same nearly symmetric profile as a moderately high excitation temperature region behind a moderately low excitation temperature region. At higher infall velocities, when the line profile is very asymmetric or has only a shoulder, the excitation temperature of the front region can be accurately determined from the red-shifted emission of that line profile. This breaks the degeneracy and creates an excitation temperature profile along the line of sight that more closely matches the simulation and is more well determined overall. As a result the physical parameters of the simulation, including the infall velocity, tend to be well determined by the TWOLAYER6 model in these cases.



In figure 20 we present a high signal to noise line profiles upon which we will carry out the procedure prescribed above. The line profile is the isolated component of an  $\text{N}_2\text{H}^+$  ( $J = 1 \rightarrow 0$ ) line profile in L1544 observed by Bourke et al. (in preparation). Based on our results in the previous sections we choose to model the emission using the HILL5 model. That best fit is shown by the points in figure 20. We see that the fit is fairly good, though it deviates from the line profile by producing a second peak instead of a shoulder. The HILL5 parameters that result in this fit are shown in table 4. In this case our HILL5 infall estimate of  $0.099 \text{ km s}^{-1}$  matches well with the best fit TWOLAYER6 estimate of  $0.095 \text{ km s}^{-1}$ . Unfortunately since we did not create this profile from a model we do not know the actual kinematic conditions in the cloud, however there are two other estimates obtained using detailed radiative transfer methods. Keto et al. (2004) have fit a model to  $\text{N}_2\text{H}^+$  ( $J = 1 \rightarrow 0$ ) and  $\text{N}_2\text{H}^+$  ( $J = 3 \rightarrow 2$ ) spectra at 4 positions around L1544. They find an infall speed profile that accelerates inwards from the cloud edge to  $0.24 \text{ km s}^{-1}$ . Although this peak infall speed is much more than our estimate, we note that their fits to L1544 include no velocity dispersion. We speculate that the infall speed may be artificially high in order to match the line width in the absence of any turbulent velocity component. Bourke et al. (in preparation) have observed this particular source in several molecular line transitions, include  $\text{N}_2\text{H}^+$  ( $J = 1 \rightarrow 0$ ),  $\text{N}_2\text{H}^+$  ( $J = 3 \rightarrow 2$ ),  $\text{DCO}^+$  ( $J = 2 \rightarrow 1$ ),  $\text{DCO}^+$  ( $J = 3 \rightarrow 2$ ),  $\text{CS}$  ( $J = 2 \rightarrow 1$ ),  $\text{CS}$  ( $J = 3 \rightarrow 2$ ),  $\text{CS}$  ( $J = 5 \rightarrow 4$ ), and  $\text{C}^{34}\text{S}$  ( $J = 2 \rightarrow 1$ ). They have used the density model of this cloud proposed by Tafalla et al. (2002) and assumed infall at the same velocity over the entire cloud along with a kinetic temperature of 10 K to create radiative transfer models of L1544 and match their observed line profiles. A simultaneous match of all the components in the  $\text{N}_2\text{H}^+$  spectral lines currently yields an infall velocity of  $0.1 \text{ km s}^{-1}$ , which is in agreement with our estimate to within a hundredth of a kilometer per second.

## 6. Conclusion

We have shown that analytic radiative transfer models are effective at estimating the infall velocities of contracting clouds from the blue-asymmetric line profiles of species of moderate optical depth in the region of collapse. The models provide good velocity estimates with few assumptions. The greatest advantage of the analytic models is that they allow for a quick and reasonable estimate of infall velocity with a minimum of computational effort. In cases where nothing else is known about the source, they provide the only possible estimate of infall, and in regions where a more robust model can be constructed, the analytic models

Table 3. Density and velocity laws of the simulated clouds

Simulation	Density Law	Velocity Law	Values
A	TMCWC	$v_{\text{in}} = a$	$a = 0.00, 0.02, \dots, 0.2 \text{ km s}^{-1}$
B	TMCWC	$v_{\text{in}} = \begin{cases} 0 & \text{if } r < r_0 \\ a & \text{if } r \geq r_0 \end{cases}$	$a = 0.00, 0.02, \dots, 0.2 \text{ km s}^{-1}$
C	TMCWC	$v_{\text{in}} = \begin{cases} a & \text{if } r < r_0 \\ 0 & \text{if } r \geq r_0 \end{cases}$	$a = 0.00, 0.02, \dots, 0.2 \text{ km s}^{-1}$
D	BE	$v_{\text{in}} = a$	$a = 0.000, 0.024, \dots, 0.24 \text{ km s}^{-1}$

Note. — The density laws are described in detail in §3. TMCWC refers to the flattened power law profile developed in Tafalla et al. (2002). BE refers to the exact solution of a hydrostatic isothermal pressure-confined self-gravitating sphere, otherwise known as a Bonnor-Ebert sphere.

Table 4. Parameters of best HILL5 fit to L1544  $\text{N}_2\text{H}^+$  profile

$\tau_0$	$v_{\text{LSR}}$ ( $\text{km s}^{-1}$ )	$v_{\text{in}}$ ( $\text{km s}^{-1}$ )	$\sigma$ ( $\text{km s}^{-1}$ )	$T_P$ (K)
3.26	7.183	0.099	0.070	6.14

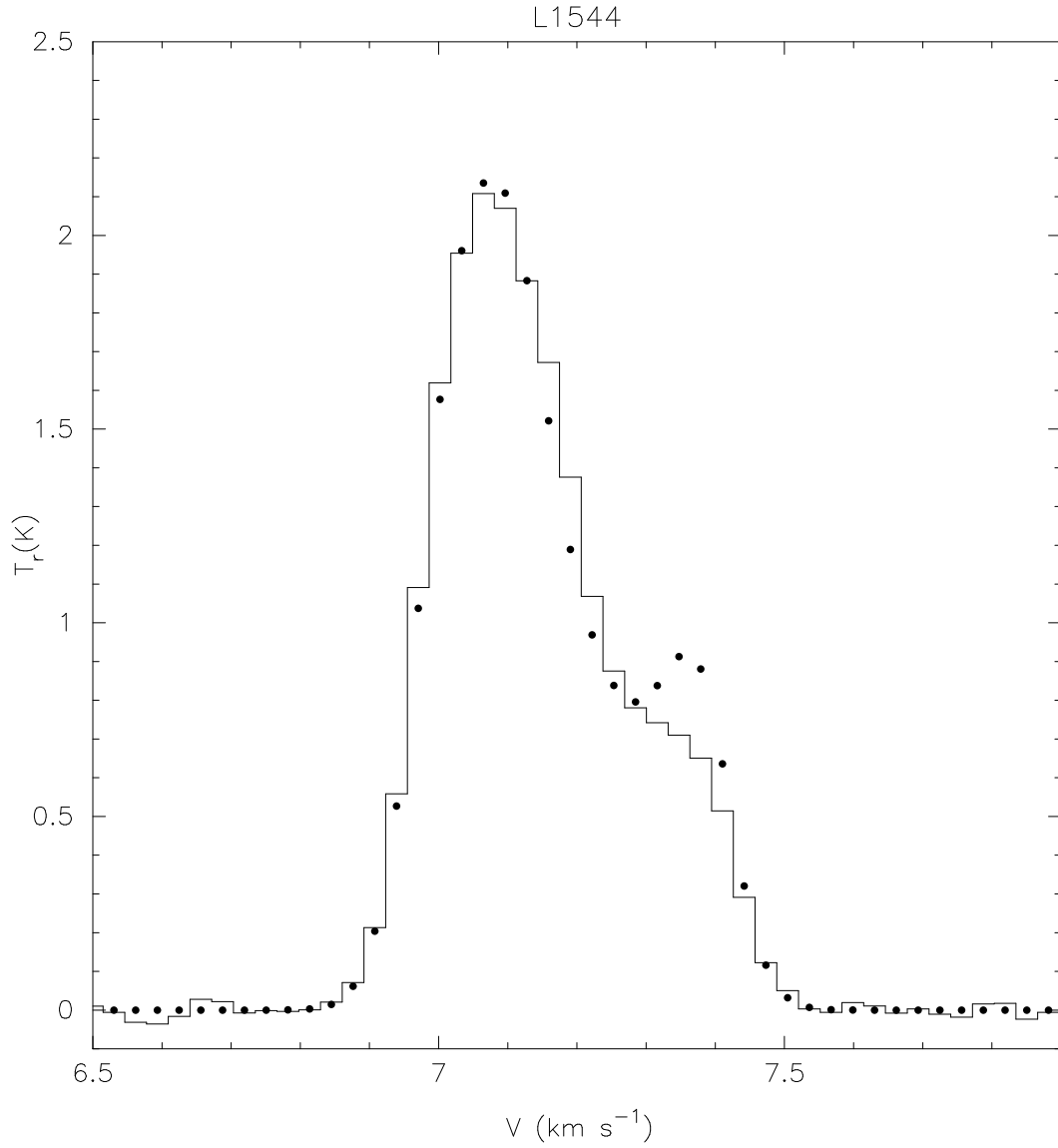


Fig. 20.— Fits of the HILL5 model to a high signal to noise  $\text{N}_2\text{H}^+$  observation of L1544. The spectrum shown is the isolated  $\text{N}_2\text{H}^+$  ( $J = 1 \rightarrow 0$ ) component observed by Bourke et al. (in preparation) toward L1544. The filled circles indicates the best HILL5 fit.

provide an excellent starting point for further modeling<sup>1</sup>. The main conclusions of this work are as follows:

1. Analytic radiative transfer models can reproduce the blue-asymmetric line profiles seen in infalling starless cores. In addition to the two-layer model first presented in Myers et al. (1996) we have found a second class of radiative transfer models (the hill models) and explored 5 variants of these two classes of analytic radiative transfer models. All the model variations were able to produce blue-asymmetric line profiles similar to those we observe in starless cores.
2. Successful analytic radiative transfer models reproduce not only the line profile shape, but also match the initial excitation conditions along the line of sight up to or beyond an optical depth of 1. When this requirement is met, the modeled infall velocity successfully fits the simulated infall velocity. Those models which match the line profile shape, but do not match the line of sight excitation conditions cannot reveal the infall velocity and velocity dispersion in the cloud.
3. The HILL5 analytic radiative transfer model is the preferred model when fitting a blue-asymmetric line profile. In simulations with constant velocity as at all cloud radii the infall velocities attained by fitting the HILL5 analytic radiative transfer model to the simulated line profiles match the infall speed with an RMS error  $0.02 \text{ km s}^{-1}$ . The HILL5 model tends to perform especially well when there are two distinct peaks such that the intensity difference between the self-absorption trough and the redshifted peak is greater than 10% of the intensity of the blueshifted peak. The RMS error in the infall determination of HILL5 fits to simulated spectral lines with those characteristics from Simulations A and D is  $0.01 \text{ km s}^{-1}$ .
4. The physical parameters of simulated clouds that produce blue-asymmetric line profiles with no distinct shoulder or redshifted peak are generally not well determined by any of the model variations we have studied in this paper. We recommend not using these models to estimate infall velocities from line profiles that do not have a separate redshifted peak or a distinct redshifted shoulder.
5. A better match to the line profile shape does not necessarily imply a better match to the excitation profile or the physical parameters, such as the infall velocity, of the observed cloud. This can be seen most clearly in figure 9 where local minimum of the

---

<sup>1</sup>Implementations of the models used for this paper are available from the authors at <http://cfa-www.harvard.edu/~cdevries/analytic.infall.html>

“dip” solution often provides a lower  $\chi^2$  fit to the line profile shape, but a poorer fit to the infall velocity than the “shoulder” solution. Following the instructions in §5 when fitting a blue-asymmetric line profile will minimize the risk of obtaining an unusually poor estimate of the physical parameters from the analytic radiative transfer model fit to the line profile.

6. All the analytic models lose sensitivity to the infall velocity if there is a significantly optically thick static envelope between the observer and the infall region. In these cases a more optically thin line can provide a better estimate to the infall velocity in the obscured region. Conversely an optically thin tracer may underestimate the infall velocity of an infalling envelope around a static cloud core. These methods are sensitive to the velocities and conditions in the regions in which the line is becoming optically thick.
7. A peak signal to noise ratio greater than or equal to 30 is required for the systematic error on the infall velocity estimate to be greater than the random error. We recommend achieving a peak signal to noise ratio of 30 in order to minimize the random error of a line profile fit using our analytic radiative transfer models, however nothing is gained by achieving a higher signal to noise level. Achieving this signal to noise level can take a prohibitively long time for lines whose peak antenna temperature is less than or equal to 1 K.
8. Depletion and beam smoothing can greatly affect the observed line profile in infalling starless cores. We conclude that, even in the presence of these effects, if the line profile is asymmetric and a good candidate to be fit using these analytic radiative transfer models (as described in §5), then generally the radiative transfer models do yield an accurate estimate of the infall velocity. If the cloud is depleted to such an extent or viewed with such a large beam that the line profile becomes very weak or symmetric, then these models will not accurately probe the infall region of the starless core.

We are grateful to Tyler Bourke for contributing his L1544 data and some preliminary results from his radiative transfer modeling for use in this paper. We also acknowledge Henrik Beuther for his encouraging advice and an anonymous referee for his or her valuable comments and suggestions. This research was conducted with support from NASA Origins of Solar Systems Grant NAG5-13050.

## REFERENCES

- Adelson, L. M. & Leung, C. M. 1988, MNRAS, 235, 349
- Alves, J., Lada, C. J., & Lada, E. A. 1999, ApJ, 515, 265
- Alves, J. F., Lada, C. J., & Lada, E. A. 2001, Nature, 409, 159
- Bachiller, R. 1996, ARA&A, 34, 111
- Bacmann, A., André, P., Puget, J.-L., Abergel, A., Bontemps, S., & Ward-Thompson, D. 2000, A&A, 361, 555
- Bacmann, A., Lefloch, B., Ceccarelli, C., Castets, A., Steinacker, J., & Loinard, L. 2002, A&A, 389, L6
- Ballesteros-Paredes, J., Klessen, R. S., & Vázquez-Semadeni, E. 2003, ApJ, 592, 188
- Barranco, J. A. & Goodman, A. A. 1998, ApJ, 504, 207
- Bergin, E. A., Ciardi, D. R., Lada, C. J., Alves, J., & Lada, E. A. 2001, ApJ, 557, 209
- Caselli, P., Benson, P. J., Myers, P. C., & Tafalla, M. 2002a, ApJ, 572, 238
- Caselli, P., Walmsley, C. M., Tafalla, M., Dore, L., & Myers, P. C. 1999, ApJ, 523, L165
- Caselli, P., Walmsley, C. M., Zucconi, A., Tafalla, M., Dore, L., & Myers, P. C. 2002b, ApJ, 565, 331
- Choi, M., Evans, N. J., Gregersen, E. M., & Wang, Y. 1995, ApJ, 448, 742
- De Vries, C. H., Narayanan, G., & Snell, R. L. 2002, ApJ, 577, 798
- Di Francesco, J., Hogerheijde, M. R., Welch, W. J., & Bergin, E. A. 2002, AJ, 124, 2749
- Green, S. 1975, ApJ, 201, 366
- Gregersen, E. M., Evans, N. J., Mardones, D., & Myers, P. C. 2000, ApJ, 533, 440
- Gregersen, E. M., Evans, N. J., Zhou, S., & Choi, M. 1997, ApJ, 484, 256
- Hogerheijde, M. R. & van der Tak, F. F. S. 2000, A&A, 362, 697
- Jessop, N. E. & Ward-Thompson, D. 2001, MNRAS, 323, 1025
- Keto, E., Rybicki, G. B., Bergin, E. A., & Plume, R. 2004, ApJ, 613, 355

- Kramer, C., Alves, J., Lada, C. J., Lada, E. A., Sievers, A., Ungerechts, H., & Walmsley, C. M. 1999, *A&A*, 342, 257
- Kuiper, T. B. H., Langer, W. D., & Velusamy, T. 1996, *ApJ*, 468, 761
- Lai, S., Velusamy, T., Langer, W. D., & Kuiper, T. B. H. 2003, *AJ*, 126, 311
- Landman, D. A., Roussel-Dupré, R., & Tanigawa, G. 1982, *ApJ*, 261, 732
- Lee, C. W. & Myers, P. C. 1999, *ApJS*, 123, 233
- Lee, C. W., Myers, P. C., & Tafalla, M. 1999, *ApJ*, 526, 788
- . 2001, *ApJS*, 136, 703
- Mardones, D., Myers, P. C., Tafalla, M., Wilner, D. J., Bachiller, R., & Garay, G. 1997, *ApJ*, 489, 719
- Monteiro, T. S. 1985, *MNRAS*, 214, 419
- Murphy, D. C. & Myers, P. C. 2003, *ApJ*, 591, 1034
- Myers, P. C., Evans, N. J., & Ohashi, N. 2000, in *Protostars and Planets IV*, ed. V. G. Mannings, A. P. Boss, & S. S. Russel (Tucson: University of Arizona Press), 217–
- Myers, P. C., Mardones, D., Tafalla, M., Williams, J. P., & Wilner, D. J. 1996, *ApJ*, 465, L133
- Narayanan, G., Moriarty-Schieven, G., Walker, C. K., & Butner, H. M. 2002, *ApJ*, 565, 319
- Narayanan, G. & Walker, C. K. 1998, *ApJ*, 508, 780
- Narayanan, G., Walker, C. K., & Buckley, H. D. 1998, *ApJ*, 496, 292
- Nelder, J. A. & Mead, R. 1965, *Computer Journal*, 7, 308
- Park, Y., Lee, C. W., & Myers, P. C. 2004, *ApJS*, 152, 81
- Shu, F. H., Adams, F. C., & Lizano, S. 1987, *ARA&A*, 25, 23
- Snell, R. L. & Loren, R. B. 1977, *ApJ*, 211, 122
- Snell, R. L., Loren, R. B., & Plambeck, R. L. 1980, *ApJ*, 239, L17
- Storn, R. & Price, K. 1997, *Journal of Global Optimization*, 11, 341

- Tafalla, M., Myers, P. C., Caselli, P., & Walmsley, C. M. 2004, *A&A*, 416, 191
- Tafalla, M., Myers, P. C., Caselli, P., Walmsley, C. M., & Comito, C. 2002, *ApJ*, 569, 815
- Tafalla, M. & Santiago, J. 2004, *A&A*, 414, L53
- van Dishoeck, E. F., Blake, G. A., Jansen, D. J., & Groesbeck, T. D. 1995, *ApJ*, 447, 760
- Whitworth, A. P. & Ward-Thompson, D. 2001, *ApJ*, 547, 317
- Willacy, K., Langer, W. D., & Velusamy, T. 1998, *ApJ*, 507, L171
- Wilner, D. J., Myers, P. C., Mardones, D., & Tafalla, M. 2000, *ApJ*, 544, L69
- Zhou, S. 1992, *ApJ*, 394, 204
- . 1995, *ApJ*, 442, 685
- Zhou, S., Evans, N. J., Kömpe, C., & Walmsley, C. M. 1993, *ApJ*, 404, 232
- . 1994, *ApJ*, 421, 854